Seeing the light: The role of cobalt in light-assisted CO_2 methanation

George E.P. O'Connell [a], Tze Hao Tan [a], Jodie A. Yuwono [b], Yu Wang [c], Amanj Kheradmand [d], Yijiao Jiang [d], Priyank V. Kumar [e], Rose Amal [a], Jason Scott [a,*], Emma C. Lovell [a,*]

[a] *Particles and Catalysis Research Group, School of Chemical Engineering, The University of New South Wales, Sydney, NSW 2052, Australia*
[b] *School of Chemical Engineering, The University of Adelaide, Adelaide, SA 5005, Australia*
[c] *Solid State and Elemental Analysis Unit, Mark Wainwright Analytical Centre, The University of New South Wales, Sydney, NSW 2052, Australia*
[d] *School of Engineering, Macquarie University, Sydney, NSW 2109, Australia*
[e] *School of Chemical Engineering, The University of New South Wales, Sydney, NSW 2052, Australia*

ARTICLE INFO

ABSTRACT

Illuminating thermal catalysts with visible light is an effective strategy to reduce the thermal requirements of CO_2 methanation. In this study, we systematically varied the cobalt loading and properties of xCo/CeO_2 catalysts (between 0 and 10 wt%) to understand changes in the visible light-assisted reaction mechanism with cobalt loading. 10Co/CeO_2 had the highest CO_2 conversion of 90% at 450 °C. The light promoted the CO_2 conversion of all catalysts from 300 to 450°C, peaking for 7.5Co/CeO_2 with a 125% improvement relative to thermal conditions (300 °C) before diminishing for 10Co/CeO_2. The light facilitated the conversion of the formate intermediate adsorbed onto CeO_2. *In-situ* DRIFTS and DFT unveiled a particle size trade-off between maximising CO_2 adsorbed at the Co-Ce interface while minimising CO_2 adsorbed onto cobalt, which is required for the best light enhancement. These findings underscore the importance of careful deposit size optimisation to unlock the light-assisted methanation's full potential.

1. Introduction

The global transition to alternative energy sources is driven by the growing socio-political attempts to curb anthropogenic CO_2 emissions, a major contributing factor to the current climate crisis. However, the inherent intermittency of renewable energy, energy storage constraints and the inadaptability to current energy and grid infrastructure hinder the shift to renewable energy, limiting its potential [1]. A promising supplement to renewable energy is the reforming of CO_2 through hydrogenation reactions, such as CO_2 methanation (Eq. 1). Here, captured CO_2 can be converted directly to methane, typically over a metal-metal oxide catalyst. Methane, as a product, is desirable for its high gravimetric energy density and compatibility with existing natural gas infrastructure. However, the energy required to overcome the stability of CO_2 and drive the reaction limits the commercialisation of CO_2 methanation [2]. Developing a catalyst for low-temperature methanation (< 400 °C) requires a comprehensive understanding of the reaction and the influence of material properties.

$$CO_2 + 4H_2 \rightleftharpoons CH_4 + 2H_2O \tag{1}$$

The methanation reaction generally follows two possible surface adsorption mechanisms: the associative and dissociative reaction pathways [3,4]. The associative reaction pathway (or the 'formate pathway') is typically characterised by the formate intermediate, where CO_2 adsorbs onto the surface as one of several possible carbonate species. Concurrently, H_2 is adsorbed and disassociated on the active metal, hydrogenating the surface carbonates into methane. Several authors have shown that surface basic sites like surface oxygen vacancies (SOVs) can aid the adsorption of CO_2 onto the support, forming the formate intermediate [3,5,6]. Alternatively, studies have shown that the formate intermediate can be formed without basic sites, where CO_2 adsorption is mediated by adsorbed oxygen species or surface hydroxyls [4,7]. The adsorbed CO intermediate (CO_{ads}) indicates the dissociative pathway, where CO_{ads} can then be directly hydrogenated or form C_{ads} before subsequent hydrogenation to produce methane [4].

A promising alternative to thermal methanation incorporates visible light (light-assisted catalysis) to offset the reaction's thermal energy requirements. Light-assisted catalysis has been shown to increase CO_2 conversion and methane selectivity through a light effect known as localised surface plasmon resonance (LSPR) [5,8]. LSPR occurs when

---

incident light causes the electrons within a nanoparticle to oscillate collectively, generating localised electromagnetic fields that aid the absorption of visible light. The absorbed light may excite an electron such that it is released to be involved in the reaction mechanism ('hot electron') or decay to release quanta of heat ('localised hotspotting')[9]. Early attempts at light incorporation utilised known 'plasmonic' materials such as Au [10,11], Ag [12] and Cu [13], which were found to promote the competing reverse water gas shift reaction (RWGS), which produces CO. More recently, several authors have demonstrated that using active metals favourable for thermal catalysis, such as Ru [14], Pd [15], Ni [5,8,16], and Co [17], was more effective. This is despite a subdued LSPR effect arising from the metal's broad light absorption range, as opposed to adsorption at specific wavelengths characteristic of plasmonic metals. These experiments were primarily performed on CeO_2 [13,16], or TiO_2 promoted with basic oxides (such as ZrO_2 [18], CeO_2 [15] and La_2O_3 [8,17]), all containing basic sites that aided CO_2 adsorption. For CeO_2, these basic sites are surface oxygen vacancies created from the facile transition between Ce^{4+} and Ce^{3+} by the delocalisation of the outer shell 4f electron [19].

Using *in-situ* diffuse reflectance infrared Fourier transform spectroscopy (DRIFTS) enables a greater understanding of how visible light impacts the reaction mechanism of basic-supported catalysts. For example, Tan et al. used a $NiO_x/La_2O_3@TiO_2$ catalyst to show that visible light stabilised the formate intermediate [8]. The authors demonstrated that without La_2O_3 promotion, the NiO_x/TiO_2 catalyst exhibited no photo enhancement. They suggested that the La_2O_3 formed a strong interaction with nickel oxide, providing proxy sites for CO_2 adsorption. This work was supported by Golovanova et al., who demonstrated that illuminating Ni/CeO_2 stimulated a 2.4-fold increase in reaction rate due to the enhanced formation and ensuing conversion of the formate intermediate on the ceria surface [16]. Recently, Ullah et al. showed that doping a TiO_2 support with lanthana provided the basic sites that stimulated the production of the formate intermediate under light-assisted conditions [17]. Ullah et al. also confirmed the relative inactivity of Co/TiO_2, confirming the need for surface basicity for light-assisted methanation. Jantarang et al. varied the surface basicity by synthesising a nickel-mixed oxide support ($Ni/Ce_xSi_yO_2$) where catalysts with different surface basicities had comparable performance under light [5]. The work suggested that ceria's SOV proximity to the active metal is more critical to the performance under light than the number of SOVs.

To date, much of the focus in this field is on elucidating the role of the catalyst support in light-assisted methanation. In contrast, no study has addressed the impact of the active metal properties on the reaction mechanism under light. A study by Kim et al. demonstrated that the plasmonic response was inferior with a small active metal size (herein referred to as 'deposit size') of < 5 nm compared to larger deposits (17.1 nm) when using a Ru/SiO_2 catalyst, although the influence of the Ru properties on the methanation mechanism was not investigated [20]. As the active metal provides the catalytic sites for the reaction to occur and the sites for visible light absorption and LSPR [9], the active metal properties such as loading, particle size and dispersion are likely to influence the light-assisted mechanism. Understanding the relationship between the active metal properties and the light-assisted mechanism is vital to further developing this field. Adjusting these properties will provide greater insight into the role of the active metal and offer an additional strategy to tune the catalyst to be more photo-responsive.

This work aims to elucidate the role of the active catalyst metal in light-assisted methanation by synthesising a novel cobalt-ceria catalyst by flame spray pyrolysis (FSP). Cobalt was selected as the active metal as it has exhibited high activity and stability under thermal conditions and demonstrated a light response for CO_2 methanation [2,17]. In line with previous studies, CeO_2 was utilised for the catalyst support to provide the basic sites required for light-assisted methanation [19,21]. FSP was employed to synthesise the Co/CeO_2 catalysts as it allows careful control of the catalyst properties. *In-situ* DRIFTS was used to identify the surface

adsorbed intermediates and determine the reaction pathway. DFT computations were employed to understand the role of visible light in disassociating H_2 on the active metal. The change in cobalt properties with loading significantly impacts catalyst activity and the extent of light assistance. The findings of this work demonstrate how visible light integration can be improved with simple changes to the catalyst while illustrating the need to consider the properties of the active metal and the support's basicity when designing a catalyst for light-assisted methanation.

2. Experimental

2.1. Synthesis

Six cobalt-ceria catalysts with varied cobalt loadings were synthesised by flame spray pyrolysis. The flame spray reactor has been previously detailed by Mädler et al. [22]. Cobalt (II) 2-ethylhexanoate (Sigma Aldrich, 65 wt% in mineral spirits) and cerium 2-ethylhexanoate (Fischer Scientific, 12% Ce in 49% 2-ethylhexanoic acid) were used as the precursors to synthesise the xCo/CeO_2 nanoparticles. The precursors were mixed with xylenes (Sigma Aldrich, reagent grade) with a constant Ce concentration (0.1 M) and varied Co amounts of x = 0, 1.25, 2.5, 5.0, 7.5 and 10 wt%. The precursor was fed to the flame at 5 mLmin^{-1} and dispersed with 5 Lmin^{-1} of O_2 (Coregas > 99.95%). The flame was maintained by a supporting flame fed by a mixture of O_2 (3.2 Lmin^{-1}) and CH_4 (0.6 Lmin^{-1}, Coregas, > 99.95%). Sheath O_2 at 5 Lmin^{-1} was used to direct the xCo/CeO_2 nanoparticles toward a filter paper/vacuum pump arrangement for recovery.

2.2. Characterisation

The catalysts were reduced and passivated *ex-situ* for selected characterisation techniques using a Micromeritics Autochem 2920. Approximately 400 mg of catalyst was supported in a quartz U-tube before reduction (20 mLmin^{-1}, Coregas 10.05% H_2 in Ar) at 550 °C for 1 h, followed by passivation in 1% O_2 in He (10 mLmin^{-1} Coregas, 0.97% O_2 in He) for 12 h at room temperature. The reduced and passivated catalysts were held under Ar (Coregas, Ar ≥ 99.9997%) to prevent reoxidation.

The specific surface area was determined using N_2 physisorption at −196 °C on a Micromeritics Tristar 3030, with the values calculated using the Brunauer-Emmett-Teller (BET) method. Prior to analysis, approximately 90 mg of catalyst was heated to 150 °C under vacuum and held for 3 h to remove surface contaminants. Inductively coupled plasma-optical emission spectroscopy (ICP-OES) was performed using a PerkinElmer Optima 7300 V to determine the cobalt loading. The samples were digested via microwave acid digestion using aqua regia (see Supplementary Information S1).

Thermal gravimetric analysis (TGA) was performed on the as-prepared and spent $10Co/CeO_2$ catalysts to identify any residual carbon from FSP synthesis and the reaction. TGA was conducted on a TGA Q5000 (TA instruments), where 3 – 4 mg of catalyst was heated to 800 °C at 20 °Cmin^{-1} in dry air (Coregas, dry air). *Ex-situ* Fourier transform infrared spectroscopy (FTIR) was performed on the CeO_2 control, as well as the as-prepared, reduced and passivated and spent $10Co/CeO_2$ catalysts using the PerkinElmer Spectrum 2 FTIR with 32 scans from 4000 to 600 cm^{-1} at a resolution of 4 cm^{-1}.

X-ray diffraction (XRD) was conducted using a Co Kα_1 X-ray source (λ_{Co} = 1.789 Å) on a PANalytical Empyrean XRD system at 45 kV and 40 mA. The spectra were obtained for $8° \leq 2\theta \leq 100°$, using a 0.026° step size at 0.01° min^{-1}. The Bragg angle associated with Co Kα_1 was converted computationally to a Cu Kα_1 Bragg angle (inferring a Cu Kα_1 source, λ_{Cu} = 1.5406 Å). The Scherrer equation was used to estimate the crystallite size (assuming K = 0.94 for this study).

Hydrogen temperature-programmed reduction (H_2-TPR) assessed the catalyst's reducibility using a Micromeritics Autochem 2920.

Between 30 and 35 mg of catalyst was loaded into a quartz U-tube. Surface-adsorbed contaminants were first removed by heating the sample to 150 °C in 20 mLmin^{-1} Ar, ramped at 5 mLmin^{-1} and held for 30 min. After returning to ambient temperature, the sample was heated to 850 °C at 10 °Cmin^{-1} in an H$_2$/Ar mixture (20 mLmin^{-1}, Coregas, 10.05% H$_2$ in Ar). The results were recorded using a thermal conductivity detector (TCD). CO-pulse chemisorption was performed on a Micromeritics Autochem 2910 to determine cobalt's active deposit size and dispersion. The catalyst was loaded into a quartz U-tube and purged in helium (20 mLmin^{-1}, Coregas, He ≥ 99.996%). The catalyst was reduced for 1 h *in-situ* by heating to 550 °C at 5 °Cmin^{-1} in 20 mLmin^{-1} of 10.05% H$_2$/Ar mixture and cooled to room temperature in He. Pulses comprising of 16.5 μmol of CO were injected until saturation was reached. Further information on the cobalt deposit size and dispersion calculation is provided in Supplementary Information S2.

A Quantachrome ChemBET Pulsar was used to assess the surface basicity by CO$_2$ temperature-programmed desorption (CO$_2$-TPD). Approximately 50 mg of catalyst was heated in 20 mLmin^{-1} He to 550 °C at 5 °Cmin^{-1} before reducing with 20 mLmin^{-1} 5% H$_2$ in N$_2$ for 1 h. Upon cooling to 40 °C in the H$_2$/N$_2$ mixture, the catalyst was purged with 20 mLmin^{-1} He for 1 h. The surface was saturated with CO$_2$ for 1 h (1% CO$_2$ in N$_2$, 20 mLmin^{-1}) before flushing with 20 mLmin^{-1} He for 1 h to remove any physisorbed CO$_2$. The sample was then heated in 20 mLmin^{-1} He to 700 °C at 5 °Cmin^{-1}.

The UV and visible light absorbance (UV-Vis) was measured using a Shimadzu UV-Vis 3600 spectrophotometer. The reflectance spectra were obtained between 200 and 950 nm for the as-prepared catalysts. The Kubelka-Munk transformation was applied to determine the absorbance. As this work is only concerned with cobalt's visible light absorption properties, ceria's band structure and semiconductor properties were not considered. Raman spectra were obtained from a Renishaw inVia microscope with an excitation wavelength of 532 nm. X-ray photoelectron spectroscopy (XPS) was conducted on a Thermo Scientific™ ESCALAB™−250Xi with Al Kα at 1486.68 eV to analyse the surface of the reduced and passivated catalysts. Adventitious carbon (284.8 eV) was used as a reference. The Ce 3d region was fitted with an iterated Shirley background with two iterations. High-resolution transmission electron microscopy (HR-TEM) was performed on the reduced and passivated catalysts using a 200 kV probe on the aberration-corrected JEOL-JEM-ARM200F electron microscope.

Transient *in-situ* DRIFTS was performed on a modified Bruker Vertex 70 V FTIR. Refer to Tan et al. for a detailed description of the experimental setup [8]. A RockSolid interferometer, liquid N$_2$-cooled MIR source and KBR optics were used for the analysis. Approximately 30 mg of catalyst was loaded into a commercial Harrick *in-situ* DRIFTS cell (Harrick Scientific, HVC-DRM-5) with a ZnSe window. A broad-range white fibre-coupled LED (ThorLabs, MCWHF-2) was attached to the cell for visible light illumination with an intensity of 40 mWcm^{-2}. The catalyst was reduced *in-situ* using a resistive heating device to heat the catalyst to 550 °C in a 1:1 ratio of Ar and H$_2$ (flow = 24 mLmin^{-1}). 24 scans with a 1 cm^{-1} resolution were recorded every 50 °C with a KBr background. After reduction, the gas was cooled to 50 °C in pure Ar, and background spectra were recorded at 50 °C intervals from 550 °C to 50 °C. The gas was changed to the reactant mixture (24 mLmin^{-1} 1:4:1 Ar, H$_2$ and CO$_2$), and the equilibrated spectra were recorded between 1000 and 4000 cm^{-1} for every 50 °C interval from 50 °C to 450 °C with the Ar background previously detailed.

Density functional theory (DFT) calculations were employed to assess the adsorption of the CO$_2$ molecule and the impact of visible light on H$_2$ adsorption and dissociation on the active metal. The calculations were performed using the Projector Augmented Wave (PAW) [23,24] method as implemented in the Vienna Ab initio Simulation Package (VASP) [25,26]. The calculations were completed with a plane-wave cut-off energy of 500 eV and Monkhorst-Pack k-points mesh of 5 × 5 × 1 (Fig. S1). The self-consistent electronic calculation was converged to 1 × 10^{-5} eV, and ionic relaxation steps were performed

using the conjugate-gradient method (IBRION = 2) and continued until the total force on each atom dropped below a tolerance of 1×10^{-2} eVÅ^{-1}. The generalised gradient approximation (GGA) was used for the exchange-correlation functionals as parameterised by Perdew-Burke-Ernzerhof (PBE) [27]. For modelling the H$_2$ adsorption, a slab method was employed for cobalt's (111) surface with a thickness of nine atomic layers and a vacuum of 20 Å in the z-direction. Bulk-surface interaction was modelled by relaxing only atoms in the three uppermost layers and fixing atoms in other layers to their bulk coordinates. The adsorptions of molecular H$_2$ and dissociated H$_2$ were then investigated by considering the number of electrons within the system, and the addition and subtraction of electrons were simulated to understand the illumination effect on the catalytic performance. The free energy diagrams for H$_2$ adsorption and dissociation were calculated by including the correction of entropy and zero-point energy, with the following steps: Co(111) + H$_2$ → Co(111)*H$_2$ → Co(111)*2H. Further modelling of the CO$_2$ adsorption modelled a CeO$_2$ (111) surface, with a thickness of nine atomic layers of Ce and O. Cobalt four-atomic cluster on top of CeO$_2$ (111) was employed to understand the influence of Co on the adsorption of CO$_2$. Dudarev's DFT+U method was included in the modelling of CeO$_2$ surfaces with an effective U = 5 eV for Ce [28].

2.3. Activity testing

Catalyst performance was assessed using a Harrick high-temperature Raman cell (Harrick Scientific HVC-MRA-5) with an 8 mm SiO$_2$ window for catalyst illumination. For the light-assisted experiments, a white LED panel (420 < λ < 710 nm) was mounted 5 mm above the aperture and maintained at 2.0 ± 0.1 Wcm^{-2} intensity. The effluent gas components were measured with both TCD and flame ionisation detector (FID) using a Shimadzu 2010 Plus gas chromatograph with a Carboplot P7 column.

For thermal testing, 14 ± 0.3 mg of catalyst was loaded into the Harrick reactor. The catalyst was reduced *in-situ* by heating to 550 °C at 5 °Cmin^{-1} in a 1:1 ratio of N$_2$/H$_2$ with a GHSV of 12 000 h^{-1} (flow = 24 mLmin^{-1}, Coregas, H$_2$ ≥ 99.99%). The sample was held at 550 °C for 1 h before being cooled at 10 °Cmin^{-1} to 150 °C. Once at 150 °C, the reactant gas mixture was introduced in a 1:4:1 ratio of N$_2$/H$_2$/CO$_2$ (flow = 24 mLmin^{-1}, GHSV = 12 000 h^{-1}). The temperature was increased by 50 °C every 45 min until 450 °C. The light was introduced with the reactant mixture at 150 °C after the *in-situ* reduction for the light-assisted tests. N$_2$ was the internal standard for scaling and calculating the CH$_4$, CO$_2$, CO and H$_2$ flow. The CO$_2$ conversion and CH$_4$ selectivity (on a CH$_4$/(CH$_4$ + CO) basis) were the metrics employed to assess the activity. The calculations are provided in Supplementary Information S4. The thermal and light-assisted catalyst stability was assessed for the 10Co/CeO$_2$ catalyst using conditions akin to the temperature-stepping profile. After *in-situ* reduction, the temperature was cooled to 350 °C at 10 °Cmin^{-1} before switching to the reactant gas mixture, where the catalyst was held for 8 h. An additional light-switching experiment was performed on the 10Co/CeO$_2$ catalyst, where the reaction switched between thermal and light-assisted conditions every 80 min throughout a stability test.

3. Results and discussion

3.1. Catalyst properties

N$_2$ adsorption/desorption isotherms were used to understand the FSP synthesised xCo/CeO$_2$ samples. The BET-specific surface area (S$_{BET}$) was greatest for the neat CeO$_2$ control at 143 m^{2}g^{-1}. Kydd et al. and Jantarang et al. observed an S$_{BET}$ of 112 m^{2}g^{-1} and 125 m^{2}g^{-1} for their FSP CeO$_2$ nanoparticles using a setup similar to this system [5,29]. The difference in S$_{BET}$ may be attributed to the greater concentration of cerium precursor used in their studies (0.5 M, compared to 0.1 M in this work). Upon cobalt introduction, the S$_{BET}$ decreased to c. 100 m^{2}g^{-1} for all samples, indicating the extent of Co-loading did not significantly vary

the ceria particle size (Table 1). Particles synthesised by FSP are typically nonporous [30]. The N$_2$ adsorption/desorption isotherms are IUPAC type II (Fig. S2)[31], whereby the hysteresis loop likely stems from inter-particle sintering, which has been observed for several other FSP-prepared nanoparticles [32,33]. TGA and *ex-situ* FTIR (Supplementary Information S6 and S7, respectively) identified some aromatic carbon residual from the synthesis in the flame, but this was removed after the reduction pretreatment step. ICP-OES determined that the cobalt loading of the catalysts was lower than the nominal loading (except for 2.5Co/CeO$_2$). The actual Co loading variation from the nominal ($\pm$ up to 30%) could be attributed to the nature of the Co precursor. The viscosity makes accurate precursor weighing difficult, but irrespective of this variation, the as-prepared particles represent a distribution of Co loadings from 0 to 10 wt%.

Catalyst crystallinity was assessed with XRD (Fig. 1a.i). The (111), (200), (220), and (311) peaks of ceria (at Bragg angles of 28.4°, 33.0°, 47.4° and 56.3°, respectively) were evident for all samples indicating that the ceria was crystalline with a face-centred cubic (FCC) structure (corresponding JCPDS card No. 78–0694). No significant peak shifts were evident for any ceria peak across all catalysts, indicating no substantial structural adjustments or strain in the ceria lattice (Fig. 1a.ii). The ionic radii of cobalt (Co^{2+} = 0.72 Å & Co^{3+} = 0.69 Å) [34] is less than cerium (Ce^{3+} = 1.01 Å & Ce^{4+} = 0.97 Å, in octahedral configuration)[35]. Therefore, direct substitutional doping of Ce with a Co atom would present as a tensile lattice strain with a reduced lattice parameter [36]. Significant changes in the lattice strain may induce surface changes like the formation of SOVs caused by the charge imbalance of the ceria [21]. Rietveld analysis revealed a negligible change in the CeO$_2$ lattice parameter upon adding cobalt, where only a small increase of up to 0.0014 Å was evident between CeO$_2$ and the xCo/CeO$_2$ catalysts (Table 1), indicating that no significant modifications were made to the bulk ceria lattice between the neat CeO$_2$ and cobalt loaded samples. Ceria crystallite sizes, determined from the Scherrer equation, are displayed in Table 1. The ceria crystallite size slightly increases upon cobalt addition (9.3 – 11.8 nm from CeO$_2$ to 1.25Co/CeO$_2$). The size remained consistent with changes in cobalt loading (11.4 – 12.4 nm). The change in the crystallite size upon adding Co is consistent with the change in S$_{BET}$, with the surface area decreasing as the crystallite size increases.

Given that, XRD was performed on the as-prepared catalysts, the surface cobalt was likely in its most oxidised form (Co$_3$O$_4$). Peaks indicative of Co$_3$O$_4$ were only evident for the 7.5Co/CeO$_2$ and 10Co/CeO$_2$ samples at 36.6° and 64.8°, corresponding to (311) and (440) planes, respectively (JCPDS No. 42–1467; Fig. S6). For loadings below 5 wt%, the cobalt crystallites were not evident. In this case, the deposits were likely below 3 nm in size and/or amorphous, which is undetectable in XRD [37]. As FSP typically produces highly crystalline cobalt oxide deposits [17], it is anticipated that the cobalt existed as small cobalt oxide crystallites less than 3 nm.

Fig. 1b depicts the reducibility of the xCo/CeO$_2$ catalysts by H$_2$-TPR. Neat CeO$_2$ exhibits a broad feature (300 – 550 °C) corresponding to the surface reduction of ceria [38]. The bulk reduction of ceria occurs from 650 °C, where the peak's tail is evident for all catalysts [38]. Four reduction peaks are evident for the Co-containing samples, except for 1.25Co/CeO$_2$, which presents three. The reducibility of the catalysts increases linearly with cobalt loading (Fig. S7), where the consumed H$_2$ reached 3.86 mmolg^{-1} for 10Co/CeO$_2$. Interestingly, the experimental H$_2$ consumed, calculated from the H$_2$-TPR curves, is greater than the theoretical H$_2$ consumption (Table 2). This difference is partly due to the surface reduction of ceria, but accounting for the 0.50 mmolg^{-1} of hydrogen consumed by the neat CeO$_2$ support, the experimental values are still c. 20% higher for 1.25, 2.5 and 5.0 wt% Co loadings, and 40% higher for 7.5 and 10 wt% Co loadings, which likely indicates cobalt-catalysed ceria reduction by hydrogen spillover. Previous work has indicated that the hydrogen spillover on reducible supports leads to facile surface oxygen vacancy generation [39,40].

Cobalt reduction typically follows two pathways: a primary pathway where Co$_3$O$_4$ reduces to CoO (the lowest energy transition) and subsequently to metallic Co^0, and a secondary pathway, whereby smaller CoO deposits reduce directly to Co^0, yielding three reduction peaks, describing the two reduction pathways [39,41]. In addition to overlapping with ceria's surface reduction peak, variations in the metal-support interaction [39,41,42], oxidation state [39], deposit size [4], and the reduction location (i.e., at the Co-Ce interface)[43] may all influence the catalyst's reducibility, causing shifts in peak positions and producing more than three peaks that make pathway identification challenging. In line with literature, each peak is designated α, β, γ, and δ in ascending temperature order for this system to facilitate comparison between samples [39]. A cobalt-ceria reducibility study by Parastaev et al. identified through *in-situ* XPS that the cobalt-catalysed ceria reduction occurred before CoO due to the strong anchoring of CoO to the support. Therefore, the γ is likely indicative of ceria reduction and δ the reduction of CoO to Co^0 [39]. In this work, the increase in γ did not necessarily correspond to a parallel reduction in another peak, further supporting this ceria reduction peak assignment. All catalysts exhibit a high-temperature reduction peak (δ), indicating a strong interaction between the CeO$_2$ support and the surface cobalt [39]. This interaction is weaker for the 2.5Co/CeO$_2$ and 5.0Co/CeO$_2$, as evidenced by the shift in the δ peak from c. 570 °C (1.25, 7.5 and 10 wt%) to c. 490 °C. As the support properties are relatively consistent across the catalysts (d$_{XRD}$, S$_{BET}$), it is reasonable to deduce that the presence of cobalt induced the metal-support interaction change. A recent xCo/CZ study demonstrated minimal peak shifting when the cobalt loading was varied (0, 1, 2.5, 5 and 10% wt%), with similar cobalt deposit sizes to this system (4.6 – 9.8 nm for Co^0), which suggests that the cobalt properties do not have a significant influence on the metal-support interaction [43]. As such, changes in the metal-support interaction is more likely due to the variances in the flame spray process.

The active cobalt deposit size and dispersion were determined by CO pulse chemisorption. Apart from the 5.0Co/CeO$_2$ catalyst, the active cobalt deposit size increases with cobalt loading, indicating that the

Table 1

Nominal and actual cobalt loading, BET specific surface area, Ce crystallite size, Ce lattice parameter and percentage of Ce^{3+} for xCo/CeO$_2$.

Catalyst	Co Loading [Dev %] (wt%)[a]	S$_{BET}$ (m^{2}g^{-1})[b]	CeO$_2$ crystallite size (nm)[c]	CeO$_2$ Lattice Parameter (Å)[d]	% Ce^{3+} (%)[e]
CeO$_2$	–	143	9.3	5.4104	20.8
1.25Co/CeO$_2$	1.56 [−25%]	106	11.8	5.4113	21.8
2.5Co/CeO$_2$	2.63 [+5%]	106	11.4	5.4111	21.2
5.0Co/CeO$_2$	3.53 [−29%]	95	12.3	5.4106	21.1
7.5Co/CeO$_2$	6.04 [−19%]	95	12.2	5.4118	21.0
10Co/CeO$_2$	9.29 [−7%]	93	12.3	5.4116	21.9

[a] Cobalt loading was obtained from ICP-OES, with [Dev %] representing the deviation from nominal loading.
[b] S$_{BET}$ was obtained from N$_2$ adsorption/desorption isotherms using BET mathematical transformation.
[c] Ceria crystallite size was calculated by the Scherrer Equation from XRD (see Supplementary Information S8).
[d] Ceria's lattice parameter obtained by Rietveld refinement of the XRD (see Supplementary Information S8).
[e] Percentage of total ceria (Ce^{3+} and Ce^{4+}) calculated from XPS.
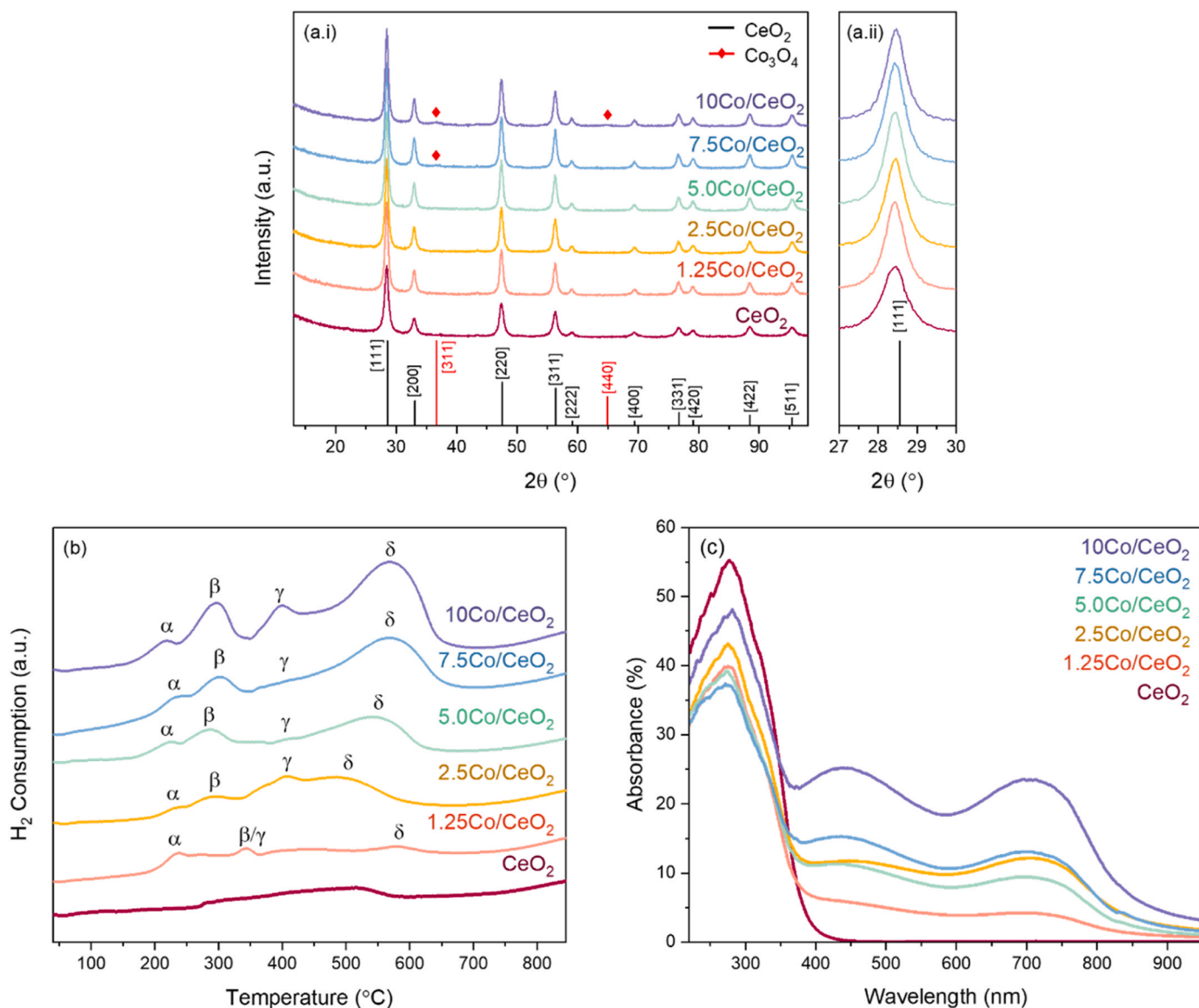
Fig. 1. (a) XRD patterns of the as-prepared xCo/CeO$_2$ (x = 0, 1.25, 2.5, 5.0, 7.5, 10 wt%) identifying (i) the full XRD spectra and (ii) the CeO$_2$ (111) phase. (b) H$_2$-TPR profiles of xCo/CeO$_2$ catalysts up to 850 °C. The peaks are denoted α, β, γ and δ, signifying the different reduction stages evident for this system. (c) UV-Vis absorbance spectra of the xCo/CeO$_2$ catalysts.

Table 2
Cobalt deposit size from CO-pulse chemisorption and TEM, surface Co concentration, Co dispersion, experimental and theoretical H$_2$ consumed.

Catalyst	Co deposit size (nm)		Co Dispersion (%)[a]	Surface Co Concentration (wt%)[c]	Experimental H$_2$ Consumed (mmolg^{-1})[d]	Theoretical H$_2$ Consumed (mmolg^{-1})[e]
	Pulse Chemisorption[a]	TEM[b] [n]				
CeO$_2$	–	–	–	0.00	0.50	0.00
1.25Co/CeO$_2$	3.3	7.9 [16]	30.2	2.49	0.92	0.35
2.5Co/CeO$_2$	5.6	8.5 [28]	17.8	2.57	1.31	0.59
5.0Co/CeO$_2$	5.1	10.8 [26]	19.5	4.81	1.74	0.80
7.5Co/CeO$_2$	9.2	10.2 [20]	10.9	8.26	2.49	1.36
10Co/CeO$_2$	12.5	12.7 [22]	8.0	9.18	3.86	2.10

[a] Active cobalt deposit size and dispersion were calculated from CO-pulse chemisorption (see Supplementary Information S2).
[b] Average cobalt sphere-equivalent diameter estimated from TEM.
[c] Surface Co concentration calculated from XPS (see Supplementary Information S9).
[d] H$_2$ consumed calculated by integrating the H$_2$-TPR profiles (Fig. 1b).
[e] Theoretical H$_2$ consumed (see Supplementary Information S9).

cobalt deposits were effectively varied with the quantity of cobalt (Table 2). The 1.25Co/CeO$_2$ sample exhibits the smallest deposit size (3.3 nm), and 10Co/CeO$_2$ has the largest size (12.5 nm). As the metallic cobalt ranged from 3.3 to 12.5 nm, the larger cobalt oxide (Co$_3$O$_4$) should be evident in XRD for all catalysts, indicating that the cobalt deposits are an assembly of smaller crystals or amorphous deposits. The 5.0Co/CeO$_2$ catalyst does not follow the trend, with a particle size akin to the 2.5Co/CeO$_2$ catalyst (5.1 nm and 5.6 nm, respectively). The dispersion is inversely proportional to the particle size, where the greatest dispersion (30.2%) is evident for the 1.25Co/CeO$_2$ catalyst, while the 10Co/CeO$_2$ has the lowest dispersion (8.0%).

UV–vis spectroscopy was conducted to identify the absorption characteristics of the as-prepared catalysts. All catalysts exhibit an absorption peak in the UV range (278 nm), corresponding to ceria's semiconductor properties (Fig. 1c)[5]. Two broad Co$_3$O$_4$ peaks at 440 nm and 710 nm are evident for each cobalt-loaded catalyst and are ascribed to the $^1A_{1g} \rightarrow {}^1T_{2g}$ and $^1A_{1g} \rightarrow {}^1T_{1g}$ energy transitions of octahedrally configured Co^{3+} [44]. The visible light absorption mainly increases with cobalt concentration, but the comparability between 2.5Co/CeO$_2$, 5.0Co/CeO$_2$, and 7.5Co/CeO$_2$ indicates that cobalt's surface concentration is not the only factor influencing visible light absorption. The 5.0Co/CeO$_2$ catalyst is the only exception to this trend, where it demonstrates a decrease in the $^1A_{1g} \rightarrow {}^1T_{1g}$ transition relative to 2.5Co/CeO$_2$. This decrease is likely attributed to the smaller cobalt size of 5.0Co/CeO$_2$ (Table 2), but other variables, such as the oxidation state, geometry, inter-particle distance and the local dielectric properties of the catalyst, may all affect the absorption properties [45,46].

HR-TEM examined the reduced and passivated catalysts to understand catalyst morphology, crystallinity, and cobalt distribution. Fig. 2a provides the micrographs of CeO$_2$, 2.5Co/CeO$_2$, and 10Co/CeO$_2$ (a.i, a.ii and a.iii, respectively). The ceria nanoparticles are highly crystalline for all catalysts, which is consistent with XRD. Cobalt deposits are evident for the 2.5Co/CeO$_2$ and 10Co/CeO$_2$. However, crystalline Co is only visible for the 10Co/CeO$_2$, not the 2.5Co/CeO$_2$ catalyst, which also agrees with the XRD results. The neat CeO$_2$ is polyhedral in shape, consistent with FSP-produced ceria [5,32]. The CeO$_2$ crystals gradually become more spherical with increasing cobalt loading (Fig. S8), which may contribute to the incremental decrease in the S_{BET} [39,41], as the surface area of polyhedral particles is greater than spherical particles. Jantarang et al. experienced similar phenomena, where CeO$_2$ underwent comparable morphology changes with increasing SiO$_2$ concentration when synthesised by FSP [5]. Fringe measurements were performed to identify changes in the lattice spacing caused by lattice strain. Measurements of the CeO$_2$ catalyst fringes identify lattice spacings of 3.0 Å and 2.7 Å, corresponding to the (111) and (200) planes of ceria, respectively [47]. For the 2.5Co/CeO$_2$ catalyst, the localised d-spacing of the (111) phase contracts (3.01 – 2.95 Å). The associated high-angle annular dark-field (HAADF) micrograph exhibits a dark spot, indicating an element of lower atomic number (i.e., cobalt) doped into the ceria lattice (Fig. 2a.ii). In recent work, Xiao et al. demonstrated that substitutional doping CeO$_2$ with Co promoted SOV formation. In their work, an XRD shift of 0.5° and a lattice parameter shift of 0.3 Å were evident for comparable catalysts (5 and 10 wt% Co) [21]. These shifts were several orders of magnitude greater than that observed for this system (Table 1), suggesting that the extent and impact of substitutional doping of cobalt into the lattice are minor for these catalysts.

Energy dispersive spectroscopy (EDS) elemental mapping identifies that cobalt is initially smaller and well dispersed for the 2.5Co/CeO$_2$
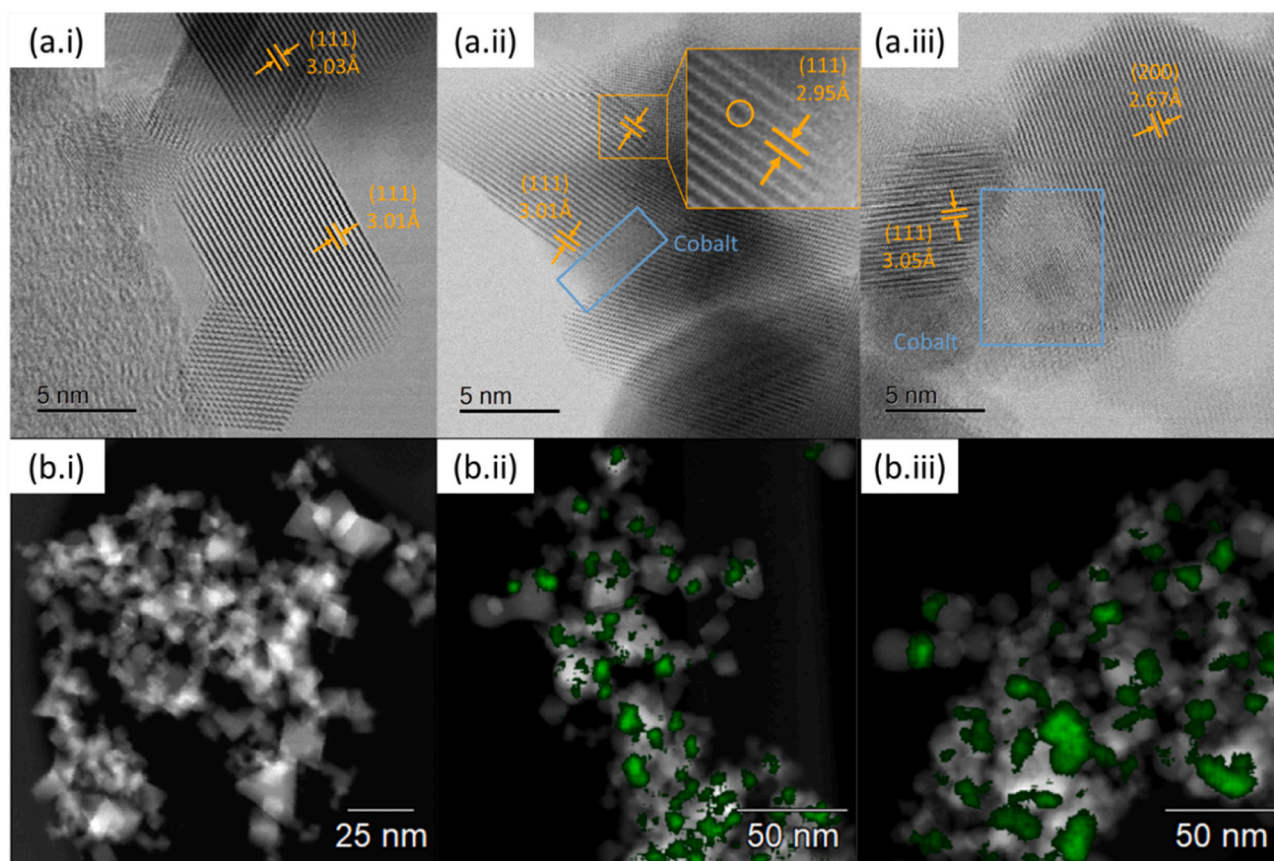
Fig. 2. (a) HR-TEM micrographs of the (a.i) CeO$_2$, (a.ii) 2.5Co/CeO$_2$ and (a.iii) 10Co/CeO$_2$ catalysts depicting the fringe measurements (yellow) and identifying the cobalt deposits (blue). The excerpt provided in (a.ii) is the HAADF-TEM of the corresponding HR-TEM, identifying a cobalt atom substitutionally doped into the ceria lattice. The scale bar represents 5 nm for all micrographs. (b) HAADF-TEM micrographs with EDS elemental mapping of cobalt (green) for (b.i) CeO$_2$, (b.ii) 2.5Co/CeO$_2$ and (b.iii) 10Co/CeO$_2$.

catalyst (Fig. 2b.ii), while much larger deposits are present for the 10Co/CeO$_2$ (Fig. 2b.iii). The cobalt frequently formed between discrete ceria crystals, binding them together (Fig. S9), which may also contribute to the decrease in S$_{BET}$ upon the addition of cobalt. The average cobalt deposit size was calculated from the deposit size distribution (Fig. S10) measured from TEM (between 16 and 28 deposits). For 10Co/CeO$_2$ and 7.5Co/CeO$_2$, the TEM particle sizes closely align with the active particle sizes determined by CO pulse chemisorption (Table 2). However, a disparity is evident for the 5.0Co/CeO$_2$, 2.5Co/CeO$_2$ and 1.25Co/CeO$_2$ catalysts. The EDS maps of these images identify a greater irregularity in the shape and size distribution of the cobalt, where smaller misshapen deposits are distributed amongst larger, more symmetrical deposits (Fig. S11). These shape and size variations likely caused the disparity between TEM and CO pulse chemisorption, as the pulse chemisorption calculation assumed spherical cobalt deposits. As the cobalt precursor concentration increases, the deposits become a collection of small cobalt crystals, as is evidenced by 7.5Co/CeO$_2$. This observation was consistent with XRD. As FSP typically produces highly crystalline nanoparticles, and small crystallites are evident in Fig. 2a.iii), it is thought that the cobalt is polycrystalline with crystals smaller than 3 nm, which are undetectable in XRD (i.e. for cobalt loading < 7.5 wt%) [33].

The surface chemistry of the reduced and passivated catalysts was explored using XPS. Ten peaks were evident for the Ce 3d spectrum (Fig. S12). Peaks representing v^0, v', u^0 and u' are attributed to surface Ce^{3+} (at 880.0, 883.7, 898.5 and 902.1 eV, respectively) whilst peaks corresponding to v, v'', v''', u, u'' and u''' are assigned to surface Ce^{4+} (at 881.9, 888.1, 897.8, 900.4, 906.9 and 916.2 eV, respectively)[48]. Substitutional doping of Ce with lower valence Co would invoke the formation of surface oxygen defects to maintain charge balance, resulting in the increased presence of Ce^{3+} (conducive of SOVs) [21]. For this system, the amount of Ce^{3+} present relative to Ce^{4+} (calculated from peak areas) is 20.8% for neat ceria, with a slight decrease upon the addition of cobalt, reaching 21.4 ± 0.5% (Table 1), indicating no significant changes in the oxidation state of the ceria surface. The variation in Ce^{3+} between the Co/CeO$_2$ catalysts is insignificant, with the lowest Ce^{3+} concentration being 21.0% for 7.5Co/CeO$_2$ and the greatest of 21.9% Ce^{3+} for 10Co/CeO$_2$. There are minor peak shifts (≤ 0.3 eV, v' peak), which follow no consistent trend between the catalysts (Table S1). The small shifts to lower binding energies for the v' and u' peaks are chemical shifts, which align with the greater proportion of Ce^{4+} present, indicative of a higher oxidation state [49].

The peaks of the Co 2p XPS were identified by literature, whereby metallic cobalt exhibits a Co 2p$_{3/2}$ peak between 778.0 and 778.5 eV, Co^{2+} has a Co 2p$_{3/2}$ peak at 780 – 781 eV with a corresponding satellite at 786 – 787 eV, and Co^{3+} had a single Co 2p$_{3/2}$ peak at 780 – 781 eV that overlapped with Co^{2+} [50,51]. The Co 2p XPS of the reduced and passivated catalysts exhibits three peaks – a Co^{3+} peak at 779.9 eV, a Co^{2+} peak at 782.1 eV and a broad satellite at 786.1 eV (Fig. 3a). The catalysts presented a low concentration of Co^{2+} (12% for 1.25Co/CeO$_2$ and c. 24% for the other catalysts, see Table S2), indicating that cobalt exists primarily in its most oxidised form of Co$_3$O$_4$, despite the reduction and passivation pretreatment, which reduced the catalyst at 550 °C for 1 h. Further investigation of the TEM micrographs for the 10Co/CeO$_2$ unveiled a cobalt oxide passivation layer around the cobalt deposit, signifying that the X-ray beam did not penetrate this layer to excite the underlying metallic cobalt (Fig. S9c). The relative amount of surface cobalt increases with the cobalt concentration, further corroborating the ICP-OES results (Table 1). An insignificant change in the binding energy of the combined Co 2p$_{3/2}$ peak (Co^{2+} and Co^{3+}) further supports the comparable oxidation state between catalysts [52]. Minor variations in the order of ± 0.2 eV are apparent for 1.25Co/CeO$_2$ and 2.5Co/CeO$_2$, which may arise from the greater signal-to-noise ratio associated with the low cobalt surface concentrations.

Raman spectroscopy was used to identify the vibrational modes of CeO$_2$ and Co$_3$O$_4$ and further probe the as-prepared xCo/CeO$_2$ catalysts (Fig. 3b). CeO$_2$ exhibits a single symmetrical F$_{2g}$ vibrational mode at 463 cm^{-1} [53–58]. As the cobalt loading increases, the F$_{2g}$ peak of ceria broadens and shifts to lower wavenumbers (to 445 cm^{-1} for 10Co/CeO$_2$). Literature suggests this redshift could be caused by phonon confinement [53], lattice strain [54] or weakening of the Ce-O force constants bond upon the addition of the active metal [55–57]. Despite evidence of lattice cobalt, Rietveld refinement identified no CeO$_2$ lattice strain for all catalysts (Table 1). Villa-Aleman et al. demonstrated that a phonon confinement shift occurred with particle size changes across two orders of magnitude (10 nm to 5 μm)[53]. As the crystallite size of ceria remains relatively consistent between the cobalt-loaded catalysts, the redshift is more likely caused by the weakening of the Ce-O bond stimulated by the electron transfer from Co to CeO$_2$ [55–57]. A broad peak at c. 600 cm^{-1} is evident for all the catalysts, corresponding to the D-band surface oxygen vacancies [58]. Only one Co$_3$O$_4$ peak is evident for these spectra, corresponding to the A$_{1g}$ one-dimensional symmetric vibrational mode at 667 – 685 cm^{-1}. An additional broad feature is evident from 450 to 650 cm^{-1}. Counterintuitively, the intensity of the cobalt peak does not appear to vary with cobalt loading, which was
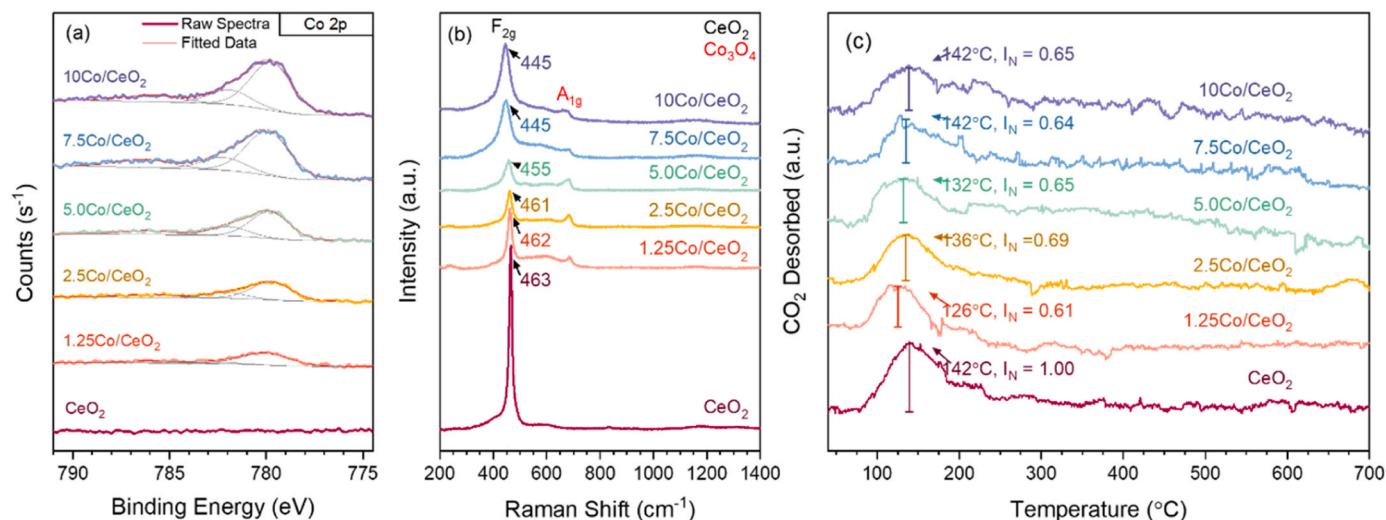
Fig. 3. (a) Co 2p XPS spectra for the reduced and passivated xCo/CeO$_2$ catalysts. (b) Raman spectra of the as-prepared xCo/CeO$_2$ catalysts, identifying ceria's F$_{2g}$ peak and subsequent peak locations (black) and cobalt's A$_{1g}$ peak (red). (c) CO$_2$-TPD of the reduced xCo/CeO$_2$ catalysts, identifying the peak positions and the intensity of the dominant peak (c. 140 °C), normalised to the CeO$_2$ peak.

observed in similar work [59]. Literature frequently reported three additional smaller cobalt peaks (two F_{2g} and one E_{1g} peaks) located between the CeO_2 F_{2g} (463 cm^{-1}) and Co_3O_4 A_{1g} peaks (685 cm^{-1}). Similar to this work, Harrison et al. also did not observe these peaks for their impregnated Co/CeO_2 where the F_{2g} and E_{1g} peaks were contained within the broad feature between the ceria F_{2g} and cobalt A_{1g} peaks, in addition to an SOV peak from 500 to 600 cm^{-1} [21,47,60]. As the broad feature from 500 to 600 cm^{-1} contains several overlapping peaks, extracting information about the SOVs is limited.

CO_2-TPD was used to assess the basicity of the reduced catalysts (Fig. 3c). All catalysts exhibit a pronounced CO_2-TPD peak at 140 °C, indicating CO_2 was weakly bound to the catalyst's basic sites (SOVs)[5]. The low-temperature peak is positively skewed, with a tail reaching c. 250 °C, indicating some variation in the strength of adsorbed CO_2. The intensity of the weakly adsorbed peak normalised to CeO_2 (I_N) was employed to facilitate comparison between catalysts. The CeO_2 has the greatest concentration of basic sites, which decreases significantly upon adding cobalt (c. 35% reduction). The intensity of the weakly adsorbed species does not change between the cobalt catalysts ($I_N = 0.65 \pm 0.04$).

However, the tail is greater for the $10Co/CeO_2$ catalysts, indicating a slightly greater concentration of medium basic sites. A H_2-temperature programmed reduction (H_2-TPR) was performed immediately after the CO_2-TPD of $10Co/CeO_2$ to gauge the extent of cobalt reoxidation after exposure to CO_2. The H_2-TPR identifies that the CO_2 reoxidised the surface cobalt by 27%, suggesting significant adsorption of CO_2 onto the surface cobalt (Fig. S13). Therefore, the basicity observed in the CO_2-TPD does not fully indicate the amount and nature of SOVs, instead reflecting a combination of SOVs and CO_2 that had oxidised the cobalt. The comparability in the CO_2 adsorption properties of the Co loaded catalysts, in addition to the amount of Ce^{3+} identified by XPS, demonstrates that ceria's reduction state is likely to be consistent across all catalysts despite evidence of cobalt-catalysed ceria reduction from H_2-TPR. Literature suggests that the catalysts with more Co can better reduce ceria due to a more reductive environment created by an increased H_2 spillover [39,40]. However, with the *in-situ* reduction conditions employed in this work (550 °C for 1 h), it is clear that Co has a greater influence on the ceria reduction rate than the reduction extent.

To summarise, six catalysts were synthesised by FSP with a
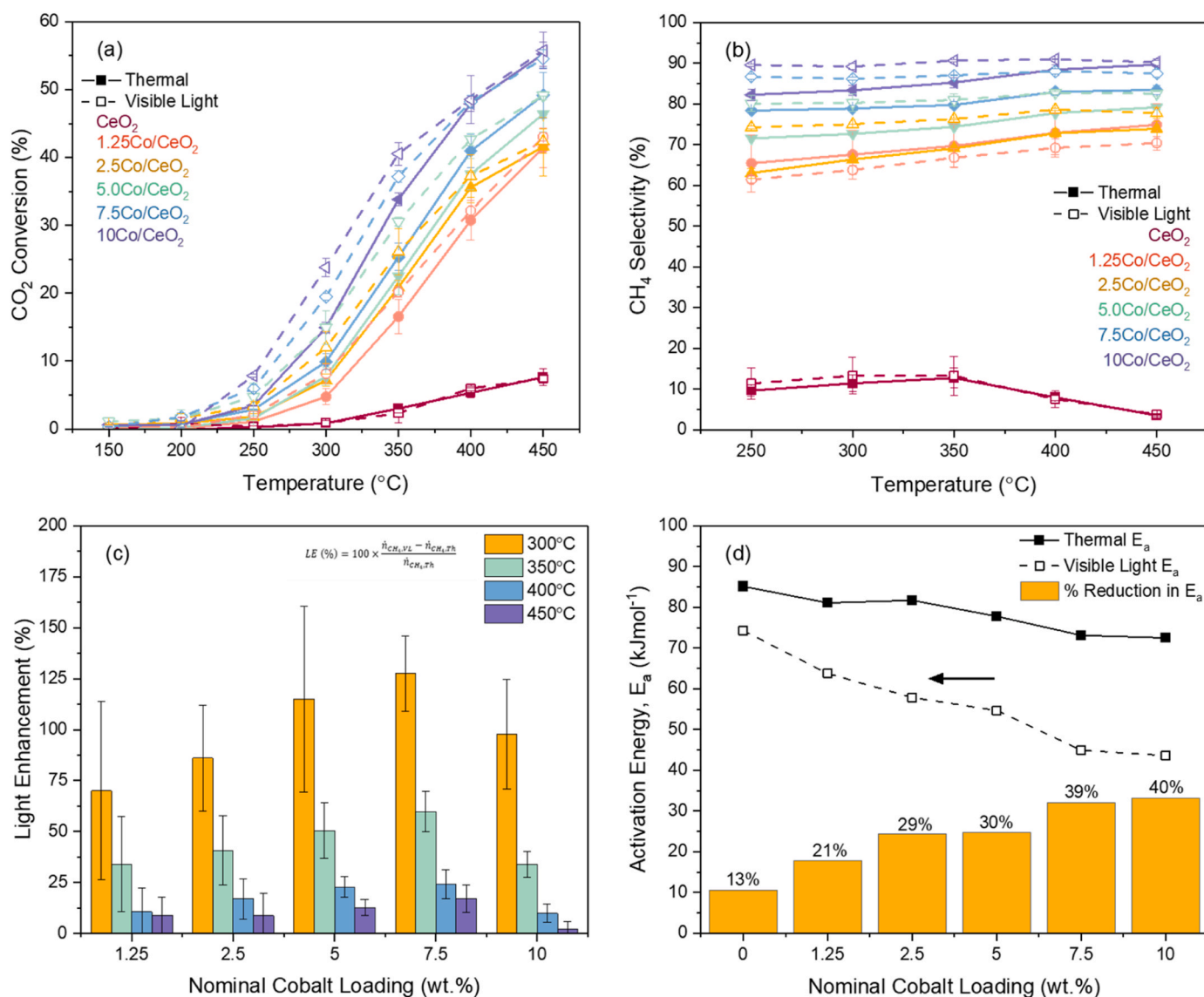
Fig. 4. Catalytic activity and selectivity exhibited by FSP xCo/CeO_2, reduced *in-situ* at 550 °C for 1 h. (a) CO_2 conversion under thermal (■) and light-assisted (□) conditions (intensity = 2.0 Wcm^{-1}). (b) Selectivity toward CH_4 under thermal and light-assisted conditions. (c) Improvement in the methane yield under visible light illumination (methane yield considers both CO_2 conversion and CH_4 selectivity). (d) Change in the activation energy between thermal and light-assisted conditions. (Reaction conditions – 150 – 450 °C, GHSV = 12 000 h^{-1}, H_2:CO_2 = 4).

distribution of actual cobalt loadings between 0 and 9.3 wt% (corresponding nominal loadings of 0 – 10 wt%). The neat ceria was highly crystalline and polyhedral in shape. The introduction of cobalt prompted a slight morphological change, whereby the particles became more spherical, and some cobalt was deposited into the ceria lattice during formation in the flame, as evidenced by TEM micrographs and corresponding fringe measurements. Rietveld refinement showed no significant change in the lattice parameter between samples, indicating that the low doping extent of cobalt had minimal impact on the bulk ceria. Despite the presence of lattice cobalt, there appeared to be no significant changes in physicochemical properties such as surface basicity (consistency of Ce^{3+} concentration and similarity between weakly adsorbed CO_2 in the CO_2-TPD), specific surface area or the CeO_2 crystallite size. There was a strong interaction between the surface cobalt and the CeO_2 support, evidenced by a fourth high-temperature reduction peak in the H_2-TPR. The active cobalt deposit size increased with loading, except for $5.0Co/CeO_2$, which was marginally less than $2.5Co/CeO_2$. There was a significant disparity between the cobalt particle sizes found by CO pulse chemisorption and measured from TEM for cobalt loadings < 7.5 wt%, which likely indicated greater ineffectiveness of adsorbing CO at lower cobalt loadings.

3.2. Visible light-assisted CO_2 methanation

Catalytic activity for the CO_2 methanation reaction was examined between 150 and 450 °C under thermal and light-assisted conditions (thermal + visible light, intensity (I_v) = 2.0 Wcm^{-1}). Under thermal conditions, the light-off reaction profile provided in Fig. 4a shows that the CO_2 conversion increases with both temperature and cobalt loading, which is consistent with literature [2,61]. The CO_2 conversion reaches a maximum of 55% for $10Co/CeO_2$ under thermal conditions at 450 °C. In contrast, the neat CeO_2 catalyst displays a limited affinity for the methanation reaction with 10% CO_2 conversion at 450 °C. The CO_2 conversion increased significantly relative to neat CeO_2 after adding cobalt, indicating that cobalt provides the active sites for the reaction. For almost all catalysts, CO_2 conversion is evident at 250 °C, below which there is minimal activity as there is insufficient energy to overcome the entropic limits of the reaction [62]. Fig. 4b demonstrates the CH_4 selectivity over CO produced from the competing RWGS reaction [2,61]. The selectivity significantly improves from c. 10% to c. 65% upon cobalt addition ($1.25Co/CeO_2$), indicating that the CeO_2 support has a much greater inclination toward producing CO. In line with the CO_2 conversion, the CH_4 selectivity improves with cobalt loading, except for $2.5Co/CeO_2$, which exhibits similar selectivity to $1.25Co/CeO_2$ (c. 64% at 250 °C and c. 74% at 450 °C). The selectivity increases with temperature for the cobalt-loaded catalysts, which varies from a 5.1% improvement for $7.5Co/CeO_2$ to 10.9% for $2.5Co/CeO_2$. Without the presence of Co, there are limited sites for the adsorption and disassociation of hydrogen (a crucial reaction step), making it more selective toward direct CO_2 disassociation into CO on CeO_2 SOVs [63].

The CO_2 conversion increased considerably upon visible light illumination for all cobalt-loaded catalysts (Fig. 4a). There is a negligible change in the activity for the neat CeO_2, likely as there are no methanation active sites, and the CeO_2 support absorbs only UV-B radiation, as shown by the UV–vis spectrum (Fig. 1c). Under visible light, almost all the cobalt-loaded catalysts are more selective toward methane production (Fig. 4b), which increases by 11.3% for $2.5Co/CeO_2$ and c. 8% for the $5.0Co/CeO_2$, $7.5Co/CeO_2$ and $10Co/CeO_2$ at 250 °C. For the better-performing catalysts (5, 7.5 and 10 wt% Co), the selectivity is not significantly influenced by temperature under light, varying by 2 – 3% from 250 to 450°C. The selectivity towards CH_4 decreases under light illumination for $1.25Co/CeO_2$, despite the greatest increase for $2.5Co/CeO_2$, indicating some sensitivity toward the reaction pathway under visible light for the low cobalt loadings.

Stability tests were performed on the $10Co/CeO_2$ catalyst at 350 °C to probe the catalytic performance further. The catalyst exhibited

greater deactivation under thermal conditions (23%) compared to visible light (16%) (Fig. S14). For CO_2 methanation, deactivation can occur through active metal sintering, carbon deposition, catalyst poisoning, and site blockage from surface-adsorbed material [3,64]. Cobalt sintering typically commences between 400 and 500 °C, and there was negligible carbon deposition throughout the reaction (Fig. S3), so the catalyst deactivation warrants further investigation. A light-switching experiment demonstrated the robustness of the light response, where the light instantaneously enhanced the methane production, achieving comparable enhancements at each illumination step (c. 10%)(Fig. S15). XRD of the spent catalysts and a second H_2-TPR was performed after the *in-situ* reduction of $10Co/CeO_2$ at 550 °C for 1 h, indicating that cobalt was in the form of Co^0 for the reaction (Fig. S16).

Fig. 4c shows the improvement in methane yield upon illumination, calculated on a thermal basis. The error bars are large, particularly at 300 °C, due to the low methane yield at low temperatures. The visible light enhancement is lowest for the $1.25Co/CeO_2$ catalyst, where the product formation increases by 61% at 300 °C. The influence of the light increases with cobalt loading until peaking for $7.5Co/CeO_2$ (128% enhancement) before decreasing for $10Co/CeO_2$. As the ceria properties are consistent across the Co loadings (surface area, basicity and crystallite size), the increased conversion and selectivity can be attributed to the change in the cobalt properties, namely the surface loading, deposit size, dispersion, and/or the metal-support interaction. Interestingly, the performance of the $5.0Co/CeO_2$ catalyst consistently sits between $2.5Co/CeO_2$ and $7.5Co/CeO_2$ despite anomalies in the particle size and visible light absorption, which indicates that the amount of surface cobalt has a substantial influence on the CO_2 methanation performance. The light enhancement trend indicates that the mechanistic influence of light is not solely dependent on the amount of cobalt present, as the enhancement extent decreases for the $10Co/CeO_2$. The impact of light diminished for all catalysts at high temperatures ($\geq$ 450 °C), with the $7.5Co/CeO_2$ achieving the greatest enhancement (17%) at 450 °C. The performance improvement for each cobalt loading under light follows the same trend from 250 to 450°C as was observed for 300 °C. It has been established in the LSPR-methanation field that the thermal pathway becomes favourable over the light-assisted pathway at higher temperatures, as the thermal energy is sufficient to convert the key reaction intermediates [5,12,17,62].

The activation energy was calculated from the Arrhenius plot provided in Fig. S17. Under thermal conditions, the activation energy is greatest for the neat CeO_2 support (85 $kJmol^{-1}$), decreasing with cobalt loading (Fig. 4d). Visible light illumination decreases the activation energy of the catalysts by 21% for $1.25Co/CeO_2$, c. 30% for $2.5Co/CeO_2$ and $5.0Co/CeO_2$ and c. 40% for $7.5Co/CeO_2$ and $10Co/CeO_2$, where $10Co/CeO_2$ decreased from 72 $kJmol^{-1}$ to 44 $kJmol^{-1}$. Recent work by Golovanova et al. observed no change in the activation energy under visible light illumination (E_a = 92.6 $kJmol^{-1}$, 0.3 < I_V < 0.5 Wcm^{-1}) when the activation energy was adjusted to corresponding local temperature increases (up to 12 °C for 0.5 Wcm^{-1} of visible light, measured by an embedded thermocouple)[16]. They concluded that the improved activity for their Ni/CeO_2 catalyst was purely from localised hotspotting caused by the decay of excited electrons. Recent work by Robatjazi et al. measured a 10 °C bulk temperature increase in an illuminated catalyst bed temperature of 200 °C and 1.1 Wcm^{-2} light intensity using an embedded thermocouple [65]. As the bulk temperature was not monitored in this work, limited conclusions could be drawn about the relative contribution of localised hotspotting or hot electrons. However, Fig. S18 shows that a catalyst bed increase of 10 °C minimally affects the activation energy for the $10Co/CeO_2$ catalyst, so light likely assists the reaction not purely by localised hotspotting but also through hot electrons generated by LSPR, indicating a dual photo-thermal pathway.

3.3. Elucidating the role of deposit size on visible light-assisted CO_2 methanation

In-situ DRIFTS and DFT studies were performed to identify the key reaction intermediates and elucidate the role of visible light in the reaction mechanism. The *in-situ* DRIFTS was performed on the 2.5Co/CeO_2 and 7.5Co/CeO_2 catalysts from 50 to 450°C under thermal and broad range visible light conditions. Only a trace of methane was evident at 250 °C (3015 cm^{-1}) in the full temperature-resolved spectra (Fig. S19), and so the DRIFTS results are provided for 100 °C, 200 °C, and 300 °C, as they describe the development of the surface adsorbed species before the reaction (100 and 200 °C), as well as changes after the reaction commenced (300 °C).

The *in-situ* DRIFTS spectra span the C-O fingerprint region (1000 – 2200 cm^{-1}) and the C-H fingerprint region (2600 – 3100 cm^{-1}). Several sources that used similar ceria catalysts were employed for the peak assignment (Table 3) [66–76]. These sources identified eight surface-adsorbed species evident for CO_2 methanation, as well as gaseous CO_2 and CH_4, depicted in Fig. 5. The C-O region evident for these Co/CeO_2 catalysts is highly saturated with various surface-adsorbed species, making peak assignment difficult. The singularly coordinated (one M – O – C bond, M = Ce or Co) bidentate carbonate (B), adsorbed CO (CO_ads), formate (F), monodentate carbonate (MC), hydrogen carbonate (HCO_3,ads, H) and methoxy (MO) peaks, the bi-coordinated bridged carbonate (Br), in addition to the tri-coordinated polydentate carbonate (P) [72], are all evident in this region. While some species are identifiable, quantitative analysis of the overlapping species is limited as peak shifts or broadening cannot be accounted for. There is less overlap in the C-H fingerprint region, which contains formate, methoxy and methane (M) vibrational modes. The formate C-H stretching vibration, ν(CH), at 2854 cm^{-1} does not overlap with other surface adsorbed materials and has thus been employed to assess trends in the adsorbed formate.

Fig. 6a and b represent the full DRIFTS spectra at 100, 200, and 300 °C under thermal and light-assisted conditions for the 2.5Co/CeO_2 and 7.5Co/CeO_2 catalysts, respectively. Both catalysts have a variety of species adsorbed on the surface. In the C-H fingerprint region, two strong formate peaks (2949 cm^{-1} and 2854 cm^{-1}), methoxy (2938 cm^{-1}) and methane's ν(CH) peak (3014 cm^{-1}) are observed. Most significantly, surface-adsorbed CO (CO_ads) is evident for both catalysts at 2000 cm^{-1}. For the DRIFTS spectra of cobalt-ceria catalysts, several authors identified that the CO_ads peak indicates CO_2 adsorbed onto surface metallic cobalt [68,77,78]. Most recently, ten Have et al. demonstrated this effect by comparing the DRIFTS spectra of CoO and Co^0 on CeO_2, whereby CO_ads were present for Co^0/CeO_2 but not CoO/CeO_2 [77]. A similar effect has been observed here, where the CO_2 in the CO_2-TPD reoxidised the cobalt, likely producing this CO_ads species. Five regions, labelled from I to V, are identified in the C-O fingerprint, each containing several overlapping peaks identified by literature. Region I contains the ν_{as}(OCO) vibrational mode of HCO_3, ads (1620 cm^{-1}), bidentate carbonate (1585 cm^{-1}) and formate (1585 cm^{-1}). Similarly, Region II has the ν_{as}(OCO) vibrational mode of monodentate (1509 cm^{-1}) and polydentate (1474 cm^{-1}) carbonates. Region III encompasses the ν_s(OCO) of HCO_3,ads (1426 cm^{-1}) and polydentate carbonate (1380 cm^{-1}), in addition to the formate COH bending mode at 1390 cm^{-1}. Region IV incorporates the OCO symmetrical stretching mode of formate (1332 cm^{-1}) and bidentate carbonate (1293 cm^{-1}). The final region, Region V, has the ν(CO) mode of polydentate, hydrogen and bidentate carbonates (1093, 1044 and 1010 cm^{-1}, respectively). Additionally, the δ(COH) mode of HCO_3,ads is evident at 1213 cm^{-1}, which does not overlap with any other peak and has subsequently been used to track this species.
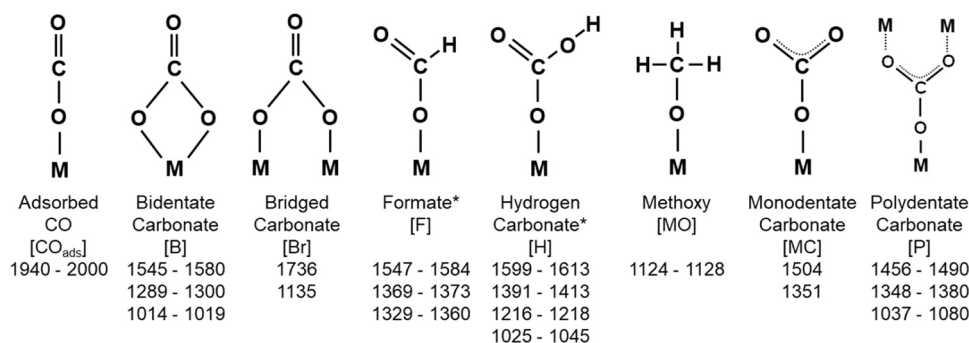
In our system, CO_ads and formate species are strongly present under thermal conditions, which are the characteristic reaction intermediates for the dissociative and associative pathways, respectively [3,4]. As the temperature increases from 200 to 300 °C, there is a considerable decline in the amount of surface adsorbed formate. Conversely, the decline in the CO_ads vibrational mode at 2000 cm^{-1} is negligible relative to the turnover of formate species, indicating that the reaction proceeds primarily via the associative pathway at this temperature. Further temperature increases prompt the conversion of CO_ads (Fig. S19) for both 2.5Co/CeO_2 and 7.5Co/CeO_2 catalysts, which illustrates that the Co/CeO_2 catalysts promote both associative and dissociative pathways simultaneously, where the formate pathway is more thermodynamically favourable due to the preferential conversion at lower temperatures (250 – 300 °C). Increasing the amount of cobalt encourages CO_ads development and invokes a considerable decrease in formate concentration, as observed in the C-H region for 7.5Co/CeO_2 at 200 °C before the reaction commenced (Fig. 6b). The change indicates that, as the cobalt loading and deposit size increases, CO_2 becomes more inclined to adsorb onto the surface cobalt (forming CO_ads) than the CeO_2 support (forming carbonyl species). Vogt et al. observed similar effects on a Ni/Al_2O_3 particle size study for thermal methanation [4]. They observed an increase in CO_ads with nickel deposit size using *operando*-DRIFTS until the surface was saturated with a monolayer of CO_ads, which prevented access to the active sites, causing poor activity at greater nickel loading (the effects commenced at 19.5 wt% Ni loading, corresponding to a 6 nm Ni deposit). In this system, the adsorbed CO species is active at higher temperatures, prompting greater performance at higher cobalt loadings. Moreover, TGA identified the presence of a small quantity of the active carbon intermediate (C_ads, Supplementary Information S6), suggesting the conversion of CO_ads into C_ads at high temperatures. For the thermal experiments up to 200 °C, there is no significant difference between the 2.5Co/CeO_2 and the 7.5Co/CeO_2 spectra in the C-O region. The resemblance of these spectra suggests that the amount of surface cobalt does not substantially impact the types of carbonates formed on the CeO_2 surface.

Upon illumination with visible light (I_V = 40 mWcm^{-2}), there is a considerable decline in the adsorbed species for 2.5Co/CeO_2 (100 °C

Table 3

Designation of DRIFTS peaks based on various literature values. All species are surface adsorbed unless otherwise stated.

| Assigned Species	Vibrational Mode: Wavenumber (cm^{-1})	Refs.
Carbonyls (C=O) and Carbonates (CO$_3$)		
Bidentate Carbonate	ν_{as}(OCO): 1545 – 1580, ν_s(OCO): 1289 – 1300, ν(CO): 1014–1019	[66–69]
Bridged Carbonate	ν_{as}(OCO): 1736, ν_s(OCO): 1135,	[38,70]
Hydrogen Carbonate	ν_{as}(OCO): 1599 – 1613, ν_s(OCO): 1391 – 1413, δ(COH): 1216 – 1218, ν(CO): 1025–1045	[66–69,71,72]
Formate	δ(CH): 2955 – 2974, δ(CH): 2735–2751, ν(CH): 2845 – 2852, ν_{as}(OCO): 1547 – 1584, δ(OCH): 1369 – 1373, ν_s(OCO): 1329 – 1360,	[66,68,69, 71–75]
Methoxy	ν_{as}(CH): 2923–2930, ν_s(CH): 2817–2832, δ(COH), ν(CO): 1124 – 1128	[74–76]
Monodentate Carbonate	ν_{as}(OCO): 1504, ν_s(OCO): 1351	[38,70]
Polydentate Carbonate	ν_{as}(OCO): 1456 – 1490, ν_s(OCO): 1348 – 1380, ν(CO): 1037 – 1080	[66,67,69]
Other Species		
Adsorbed CO (CO$_{ads}$)	ν(CO): 1940–2000	[68,69]
Gaseous CO_2	ν(CO): 2200 – 2400	[68,69]
Gaseous CH_4	ν(CH): 3016, δ(CH): 1305	[68,69]

Fig. 5. Chemical structure of the dominant surface adsorbed species. The adsorption regions provided correspond to the C-O fingerprint region (1000 – 2000 cm^{-1}). The '*' for formate and hydrogen carbonate denotes the possibility of bidentate formate and bidentate hydrogen carbonate, whereby the C=O bond coordinates with an additional surface metal atom (Ce or Co), denoted 'M'.
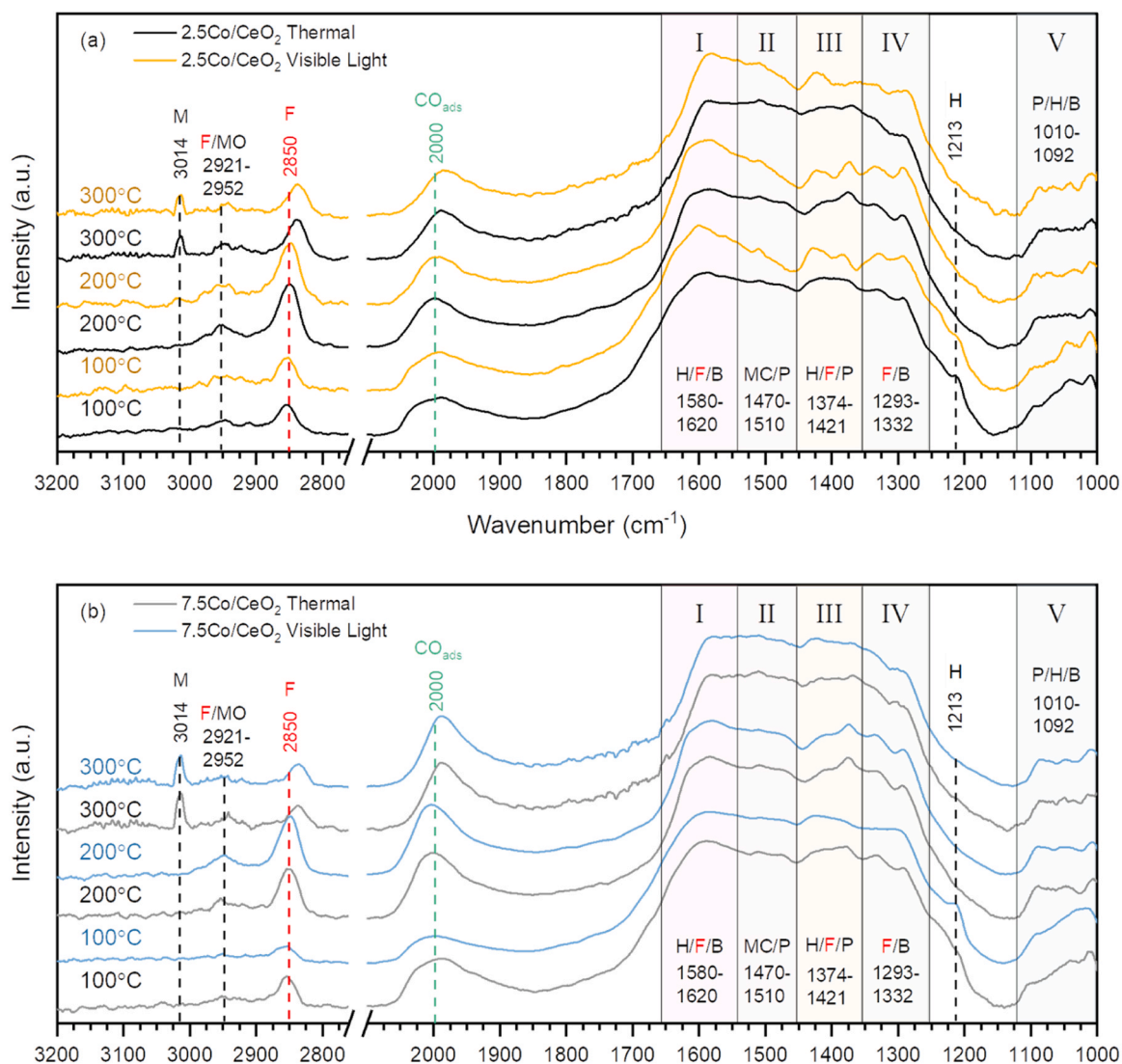
Fig. 6. (a) The *in-situ* DRIFTS spectra of the 2.5Co/CeO$_2$ catalyst under thermal (black) and light-assisted (yellow) conditions from 100 to 300°C. (b) The *in-situ* DRIFTS spectra of the 7.5Co/CeO$_2$ catalyst under thermal (black) and light-assisted (blue) conditions. Five regions were identified in the C-O region (labelled I to V) to aid the comparison of the saturated spectra. All peaks were normalised to the 7.5Co/CeO$_2$ light-assisted gaseous CO$_2$ peak to facilitate the comparison (2336 cm^{-1} - see Fig. S19 for the full spectrum). 'B' = bidentate carbonate, 'CO$_{ads}$' = adsorbed CO (green), 'F' = formate (red), 'H' = hydrogen carbonate (bicarbonate), 'M' = methane, 'MC' = monodentate carbonate, 'MO' = methoxy and 'P' = polycarbonate.
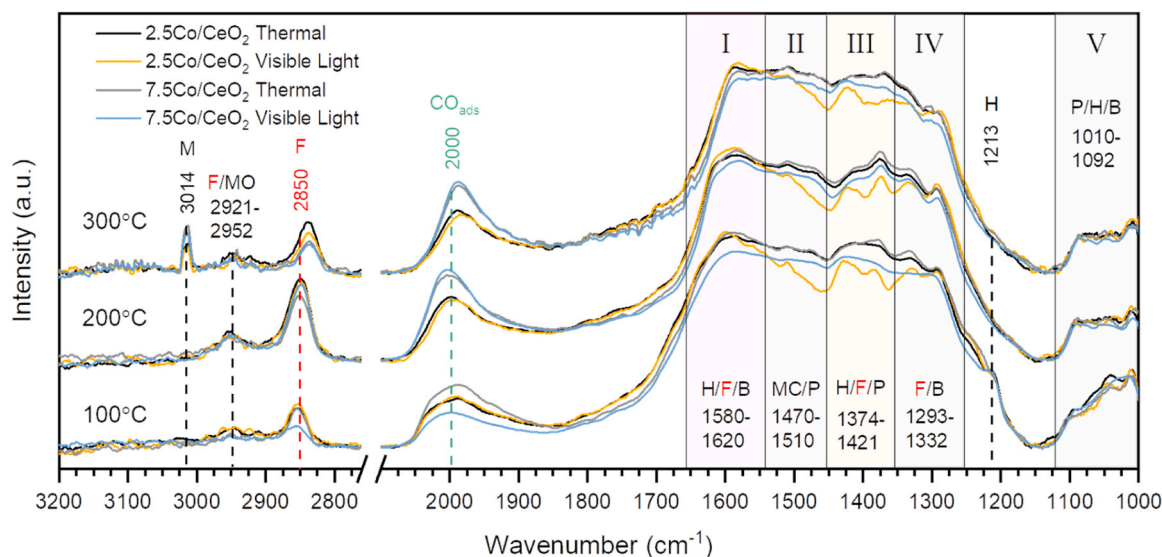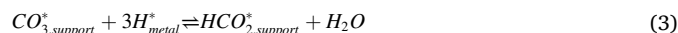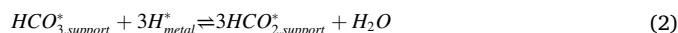
Fig. 7. Overlaid DRIFTS spectra at 100, 200, and 300 °C illustrating the impact of visible light illumination on the thermal methanation reaction over Co/CeO$_2$. Black = thermal 2.5Co/CeO$_2$, yellow = light-assisted 2.5Co/CeO$_2$, grey = thermal 7.5Co/CeO$_2$ and blue = light-assisted 7.5Co/CeO$_2$.

and 200 °C). There is no apparent change in the formate signature ν(CH) mode at 2854 cm^{-1}, indicating that light does not facilitate the formate intermediate's low-temperature formation for the smaller deposit sizes. In the C-O domain, reductions in the II, III and IV regions are evident before the reaction commences (i.e., at 100 and 200 °C). At 100 °C, HCO$_{3,ads}$ is evident (1213 cm^{-1}), disappearing by 200 °C, indicating that the HCO$_{3,ads}$ species is highly active. As formate and HCO$_{3,ads}$ are consistent with the thermal spectrum at 100 °C, it is therefore likely that the visible light limits the formation or facilitates the low-temperature conversion of polydentate carbonate, causing the significant reductions observed in Regions II and III. The only increase in surface adsorbed species is evident in Regions I and IV, likely corresponding to bidentate carbonate formation (as formate and HCO$_{3,ads}$ exhibit minimal changes from thermal conditions). The decrease in polydentate species may reflect its conversion into bidentate carbonate, a more active reaction intermediate [72].

The total amount of adsorbed species in Regions I to V in the C-O domain decreases for 7.5Co/CeO$_2$ upon illumination. Unlike the 2.5Co/CeO$_2$ catalyst, the relative peak sizes remain consistent across the C-O region, indicating that visible light has a minimal effect on the surface intermediates (Fig. 7). A small increase in CO$_{ads}$ suggests that the absorbed light facilitates CO$_2$ adsorption onto the cobalt deposit rather than solely the support for 7.5Co/CeO$_2$, indicating that the light is better at activating the Co rather than the CeO$_2$ support. Within the C-H region, the light-assistance greatly improves surface formate formation (ν(CH) = 2853 cm^{-1}), where its concentration is similar to 2.5Co/CeO$_2$ (Fig. 7). This phenomenon is described by Tan et al., who observed a comparable increase in formate formation under visible light before the reaction commenced. Their analysis described how the light activated the formate intermediate, stimulating its conversion, which was regarded as the rate-limiting step of the associative pathway [8]. For this system, the decrease in the activation energies indicates that the light facilitates the activation of the key reaction intermediates. Here, 7.5Co/CeO$_2$ exhibits a greater reduction in activation energy than 2.5Co/CeO$_2$ (39% compared to 29% for 2.5Co/CeO$_2$ (Fig. 4d), likely arising from the notably improved low-temperature (200 °C) production of formate for 7.5Co/CeO$_2$. However, if the light promotes formate formation and subsequent conversion, then an increase in formate concentration at 200 °C should also be evident for 2.5Co/CeO$_2$, as both catalysts possess comparable surface adsorbed species (indicating similar reaction mechanisms). Previous literature reported that formate formation for the associative pathway frequently involves the hydrogenation of HCO$_3$,
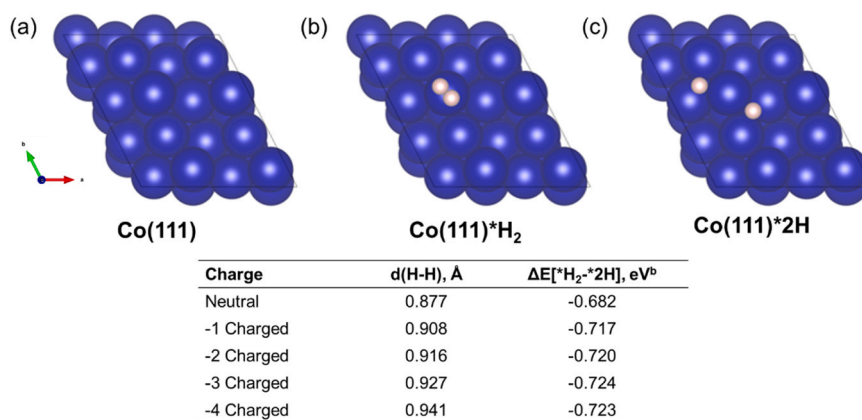
$_{ads}$ and surface carbonates (Eqs. 2 and 3, respectively) at the support-active metal interface [8,79]. As the active metal is widely accepted as the H$_2$ disassociation site, limiting the amount of active metal would limit this crucial reaction step [3,4]. As no formate promotion is evident for 2.5Co/CeO$_2$, it is thought that visible light promoted H$_2$ disassociation on the active metal, which drives the two formate formation reactions.

$$HCO^*_{3,support} + 3H^*_{metal} \rightleftharpoons 3HCO^*_{2,support} + H_2O \tag{2}$$

$$CO^*_{3,support} + 3H^*_{metal} \rightleftharpoons HCO^*_{2,support} + H_2O \tag{3}$$

After the reaction commenced (i.e. at 300 °C), both the peaks in Region IV, representing the bidentate carbonate and formate species, decreased for 2.5Co/CeO$_2$ and 7.5Co/CeO$_2$, indicating that the hydrogenation of formate and bidentate carbonate at the Co-Ce interface are both elementary steps for this reaction, which agrees with literature [8]. There is also a decrease in the methoxy intermediate, suggesting the rapid conversion into methane (ν(CH) = 2921 cm^{-1}). There appear to be no changes in Region II, indicating that polydentate and monodentate carbonate concentrations are not active species. After purging the catalyst with Ar at 450 °C, the polydentate carbonate remains, indicating that the species is strongly adsorbed to the catalyst surface (Fig. S20). Peaks corresponding to the bridged carbonate intermediate also remain, indicating that the coordination of more than one oxygen to a metal atom (M = Ce or Co) is highly stable and, therefore, inactive within this temperature range (up to 450 °C). In addition to the 2.5Co/CeO$_2$ and 7.5Co/CeO$_2$ catalysts, *ex-situ* FTIR identified the adsorbed polydentate carbonate species on the 10Co/CeO$_2$ spent catalysts, suggesting the strongly adsorbed species is present for all catalysts (Fig. S4) and was not evidenced by the CO$_2$-TPD as the adsorption strength exceeded the measurable temperature limit (750 °C). Several authors have shown that the formation of polydentate carbonates led to a decrease in the catalyst stability by blocking reactive sites [64,80]. In this system, we attribute the deactivation to the build-up of polydentate carbonate. This effect is limited under visible light, as the light inhibited the formation of these polydentate species, which resulted in improved catalytic stability.

Under thermal conditions, both catalysts exhibit a rapid conversion of the formate intermediate. The conversion rate is improved considerably upon illumination, where the extent of formate conversion is greater for 7.5Co/CeO$_2$ (Fig. 6), in line with the extent of light enhancement observed for the activity results (Fig. 4c). For both

Charge	d(H-H), Å	ΔE[*H₂-*2H], eV[b]
Neutral	0.877	-0.682
-1 Charged	0.908	-0.717
-2 Charged	0.916	-0.720
-3 Charged	0.927	-0.724
-4 Charged	0.941	-0.723

Fig. 8. Model used in DFT calculations showing the (111) phase of metallic cobalt with (a) no surface adsorbed material, (b) an adsorbed H_2 molecule and (c) a dissociated H_2 molecule. The table describes the change in the H-H bond length (d, Å) and the free energy of the disassociation reaction $\Delta E[*H_2 - *2H]$.

catalysts, there is negligible change in the CO_{ads} under thermal conditions, although, upon illumination, some CO_{ads} reacted (at 300 °C), indicating that a small portion of the absorbed light is redistributed onto the cobalt deposit, aiding the adsorption and subsequent conversion of CO_{ads}. As the two competing pathways are present, it is clear that the light enhanced the associative pathway.

DFT modelling assessed the CO_2 molecule's binding strength on the catalyst surface. The adsorption was modelled on a defective CeO_2 (111) surface with a single surface oxygen vacancy (Fig. S21a), a pure Co^0 (111) surface (Fig. S21b), and finally, a defective CeO_2 (111) surface with a small Co^0 (111) deposit to assess the adsorption of CO_2 when influenced by both cobalt and ceria (Fig. S21c). The CO_2 adsorption binding strength of unsupported cobalt ($E_{ads} = +3.09$ eV) indicated that CO_2 cannot adsorb onto the Co^0 surface. The CO_2 adsorption energy on Co-Ce ($E_{ads} = -0.30$ eV) was greater than that of the neat defective CeO_2 surface ($E_{ads} = -0.63$ eV), indicating that CO_2 preferentially adsorbs onto the CeO_2, which is paramount to the associative pathway.

The role of visible light in enhancing hydrogen turnover was further probed with DFT calculations. Light illumination was modelled by introducing additional electrons to the Co surface, mimicking the production of hot electrons via LSPR. Firstly, the adsorption of an H_2 molecule was modelled on the (111) plane of metallic cobalt. We found

that an increase in the H-H bond length of the $*H_2$ molecule on the Co (111) surface with the addition of electrons indicates that hot electrons weaken the H-H bond. This bond length increase suggests improved H_2 dissociation on the surface in the presence of light. Following this, the free energy for the dissociation reaction ($\Delta E[*H_2 - 2H]$) was evaluated, showing that the dissociated H-H state becomes more favourable with additional electrons. This energy difference increases from -0.682 to -0.717 eV under one hot electron, demonstrating that the hot electrons could favour the dissociation of H_2 on the surface. The improved dissociation of the H_2 molecule under light closely agrees with the observations from the DRIFTS experiments.

The extent of the light enhancement is prone to both the particle size effect and the amount of light absorbed. The $7.5Co/CeO_2$ *in-situ* DRIFTS demonstrates that as the particle size increased, more CO_2 adsorbed onto cobalt, producing the CO_{ads} intermediate. Despite this, the $7.5Co/CeO_2$ catalyst exhibited the greatest light response. However, the impact of the light decreases significantly for the $10Co/CeO_2$ despite more surface cobalt and greater thermal activity. We propose that there exists a novel particle size trade-off for this system. As the particle size increased, more CO_2 was adsorbed onto the cobalt, which formed CO_{ads} despite DFT confirming that it is less favourable than the CeO_2 surface. This, in turn, changes the relative contribution of the associative and dissociative
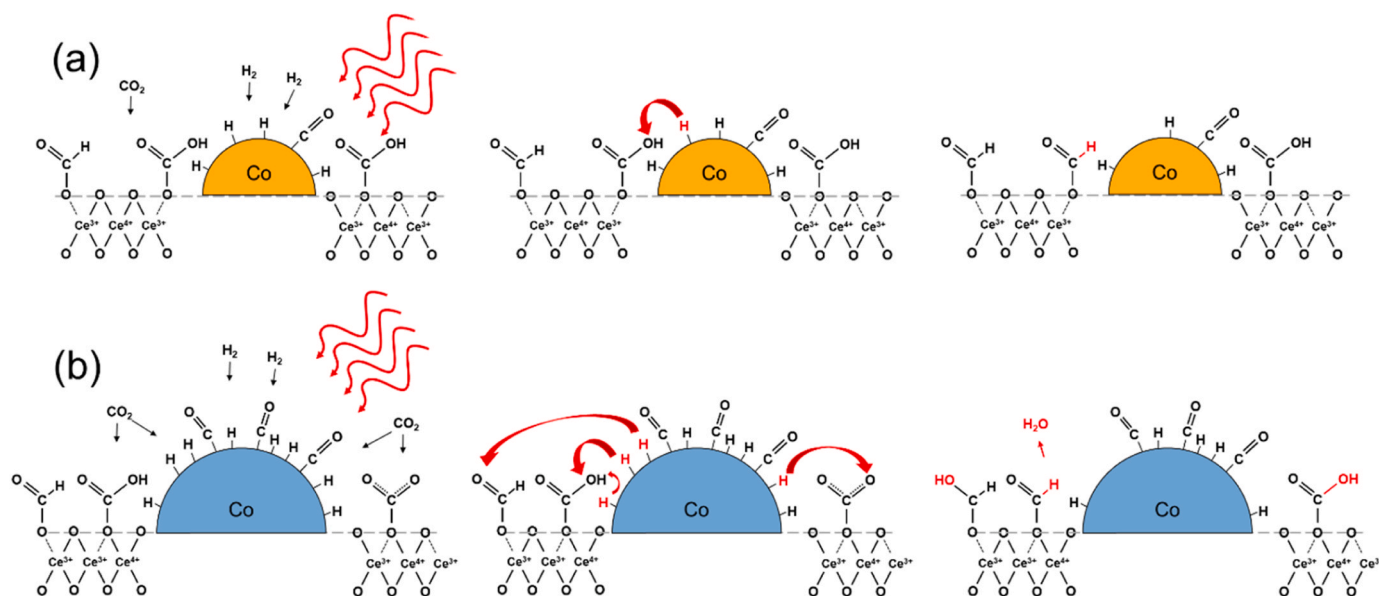
Fig. 9. Proposed light-assistance scheme for (a) $2.5Co/CeO_2$ and (b) $7.5Co/CeO_2$. The light facilitates H_2 disassociation and spillover for the hydrogenation of important surface intermediates, which is limited for $2.5Co/CeO_2$ by the particle size. The formate intermediate ($*HCO_2$) is then further hydrogenated to form CH_4.

reaction pathways. As the light enhances the formate pathway, an increased amount of adsorbed CO caused by larger particle sizes diminishes the role of the light, thereby limiting its function. Conversely, for smaller deposits of Co, *in-situ* DRIFTS showed that the CO_2 is more likely to form carbonates and the formate intermediate due to greater availability of ceria oxygen vacancies at the Co-Ce interface. This elucidates a delicate interplay between increasing the particle size to maximise the SOVs available for hydrogenation at the Co-Ce interface, achieving a superior activity enhancement by visible light and restricting the particle size to limit the adsorption of CO_2 onto cobalt, which is unresponsive to the visible light relative to the CO_2 adsorbed onto CeO_2. We propose a light-assisted methanation mechanism in Fig. 9, where CO_2 adsorbs on both the CeO_2 surface, forming carbonyl species (such as *HCO_3 and formate) and onto the metallic cobalt, where more is absorbed with a greater amount of cobalt. Under visible light, the disassociation of H_2 is promoted, creating *H that spills over to hydrogenate the intermediate carbonyl species at the Co-Ce interface and produce methane.

4. Conclusions

In this work, the cobalt loading of Co/CeO_2 was systematically increased from 0 to 10 wt% (nominal) by FSP to examine the influence of the active metal on the light-assisted conversion of CO_2 to methane. Characterisation of the cobalt deposits showed that the particle size, visible light absorption properties and metal-support interaction changed with cobalt loading. In contrast, the properties of CeO_2 experienced no significant changes despite evidence of cobalt doping within the ceria lattice. Furthermore, there were no significant changes in the surface basicity between the catalysts, which has been established in literature as the CO_2 adsorption sites for the associative methanation pathway.

The Co/CeO_2 catalysts were active and selective for CO_2 methanation, whereby the CO_2 conversion increased with cobalt loading. Illumination with visible light greatly improved the CO_2 conversion and CH_4 selectivity for all catalysts, attaining up to a 125% enhancement for $7.5Co/CeO_2$. *In-situ* DRIFTS revealed that the Co/CeO_2 followed both associative and dissociative pathways. The relative contribution of the dissociative pathway increased with cobalt loading, as the adsorption of the characteristic intermediate, CO, onto the cobalt deposit became more likely with greater deposit size. Despite the competitive reactions, the associative pathway was the dominant reaction pathway, as CO_{ads} began converting effectively at 400 °C. A reaction scheme was proposed where illumination with visible light enhances the formation and subsequent conversion of the formate intermediate at the cobalt-ceria interface. The *in-situ* DRIFTS showed that the light stimulated the formate formation for $7.5Co/CeO_2$ but not for $2.5Co/CeO_2$, signifying that the light drives the H_2 turnover on the active metal, which in turn drives the conversion of the carbonyl intermediates of the associative pathway. DFT modelling confirmed these results, whereby the light specifically promoted the disassociation of the H_2 molecule, which in turn created a proton-rich environment that drove the hydrogenation of the key reaction intermediates of the associative pathway. Future work must find a balance between (i) maximising the H_2 turnover and light response by increasing the cobalt loading and (ii) restricting the cobalt loading to limit the CO_2 adsorption onto the cobalt, thereby limiting the contribution of the dissociative pathway, which is the unfavourable light-assisted methanation pathway. In doing so, the incorporation of visible light can greatly offset the thermal requirements for the methanation reaction, further paving the way for solar-driven CO_2 valorisation.

CRediT authorship contribution statement

George E.P. O'Connell, Emma C. Lovell, Jason Scott, and **Rose Amal** designed the project and experiments. **George E.P. O'Connell**

synthesised the materials, in addition to characterisation, activity tests and data analysis, with inputs from **Emma C. Lovell, Jason Scott,** and **Rose Amal**. **George E.P. O'Connell** and **Tze Hao Tan** performed the DRIFTS analysis. **Jodie A. Yuwono** and **Priyank V. Kumar** performed the DFT calculations and assisted with the manuscript write-up of the corresponding sections. **Yu Wang** performed the Rietveld analysis. **Amanj Kheradmand** and **Yijiao Jiang** performed the CO_2-TPD experiments. **George E.P. O'Connell** wrote the manuscript, and **Emma C. Lovell, Tze Hao Tan, Jason Scott,** and **Rose Amal** edited and commented on the manuscript. **George E.P. O'Connell** prepared the graphical abstract. All authors who contributed to this work discussed the results and declared no conflict of interest.

Declaration of Competing Interest

The authors declare that they have no known competing financial interests or personal relationships that could have appeared to influence the work reported in this paper.

Data availability

Data will be made available on request.

Appendix A. Supporting information

Supplementary data associated with this article can be found in the online version at doi:10.1016/j.apcatb.2023.123507.

References

[1] R.B. Jackson, P. Friedlingstein, R.M. Andrew, J.G. Canadell, C. Le Quéré, G. P. Peters, Persistent fossil fuel growth threatens the Paris Agreement and planetary health, Environ. Res. Lett. 14 (2019) 121001, https://doi.org/10.1088/1748-9326/ab57b.

[2] W.J. Lee, C. Li, H. Prajitno, J. Yoo, J. Patel, Y. Yang, S. Lim, Recent trend in thermal catalytic low temperature CO_2 methanation: a critical review, Catal. Today 368 (2021) 2–19, https://doi.org/10.1016/j.cattod.2020.02.017.

[3] L. Shen, J. Xu, M. Zhu, Y.-F. Han, Essential role of the support for nickel-based CO_2 methanation catalysts, ACS Catal. 10 (2020) 14581–14591, https://doi.org/10.1021/acscatal.0c03471.

[4] C. Vogt, E. Groeneveld, G. Kamsma, M. Nachtegaal, L. Lu, C.J. Kiely, P.H. Berben, F. Meirer, B.M. Weckhuysen, Unravelling structure sensitivity in CO_2 hydrogenation over nickel, Nat. Catal. 1 (2018) 127–134, https://doi.org/10.1038/s41929-017-0016-y.

[5] S. Jantarang, E.C. Lovell, T.H. Tan, B. Xie, J. Scott, R. Amal, Altering the influence of ceria oxygen vacancies in $Ni/CexSiyO2$ for photothermal CO_2 methanation, Catal. Sci. Technol. 11 (2021) 5297–5309, https://doi.org/10.1039/D1CY00136A.

[6] M. Zhu, P. Tian, M. Cao, J. Chen, T. Pu, B. Shi, J. Xu, J. Moon, Z. Wu, Y.-F. Han, Vacancy engineering of the nickel-based catalysts for enhanced CO_2 methanation, Appl. Catal. B 282 (2021) 119561, https://doi.org/10.1016/j.apcatb.2020.119561.

[7] Q. Pan, J. Peng, T. Sun, S. Wang, S. Wang, Insight into the reaction route of CO_2 methanation: promotion effect of medium basic sites, Catal. Commun. 45 (2014) 74–78, https://doi.org/10.1016/j.catcom.2013.10.034.

[8] T.H. Tan, B. Xie, Y.H. Ng, S.F.B. Abdullah, H.Y.M. Tang, N. Bedford, R.A. Taylor, K.-F. Aguey-Zinsou, R. Amal, J. Scott, Unlocking the potential of the formate pathway in the photo-assisted Sabatier reaction, Nat. Catal. 3 (2020) 1034–1043, https://doi.org/10.1038/s41929-020-00544-3.

[9] M. Ghoussoub, M. Xia, P.N. Duchesne, D. Segal, G. Ozin, Principles of photothermal gas-phase heterogeneous CO_2 catalysis, Energy Environ. Sci. 12 (2019) 1122–1142, https://doi.org/10.1039/C8EE02790K.

[10] H. Liu, M. Li, T.D. Dao, Y. Liu, W. Zhou, L. Liu, X. Meng, T. Nagao, J. Ye, Design of PdAu alloy plasmonic nanoparticles for improved catalytic performance in CO_2

reduction with visible light irradiation, Nano Energy 26 (2016) 398–404, https://doi.org/10.1016/j.nanoen.2016.05.045.

[11] H. Song, X. Meng, T.D. Dao, W. Zhou, H. Liu, L. Shi, H. Zhang, T. Nagao, T. Kako, J. Ye, Light-enhanced carbon dioxide activation and conversion by effective plasmonic coupling effect of Pt and Au nanoparticles, ACS Appl. Mater. Interfaces 10 (2018) 408–416, https://doi.org/10.1021/acsami.7b13043.

[12] I. García-García, E.C. Lovell, R.J. Wong, V.L. Barrio, J. Scott, J.F. Cambra, R. Amal, Silver-based plasmonic catalysts for carbon dioxide reduction, ACS Sustain Chem. Eng. 8 (2020) 1879–1887, https://doi.org/10.1021/acssuschemeng.9b06146.

[13] S. Ullah, E.C. Lovell, R.J. Wong, T.H. Tan, J. Scott, R. Amal, Light-enhanced CO_2 reduction to CH_4 using nonprecious transition-metal catalysts, ACS Sustain Chem. Eng. 8 (2020) 5056–5066, https://doi.org/10.1021/acssuschemeng.9b06823.

[14] L. Lin, K. Wang, K. Yang, X. Chen, X. Fu, W. Dai, The visible-light-assisted thermocatalytic methanation of CO_2 over Ru/TiO(2-x)Nx, Appl. Catal. B 204 (2017) 440–455, https://doi.org/10.1016/j.apcatb.2016.11.054.

[15] N. Li, X. Zou, M. Liu, L. Wei, Q. Shen, R. Bibi, C. Xu, Q. Ma, J. Zhou, Enhanced visible light photocatalytic hydrogenation of CO_2 into methane over a Pd/Ce-TiO2 nanocomposition, J. Phys. Chem. C. 121 (2017) 25795–25804, https://doi.org/10.1021/acs.jpcc.7b07298.

[16] V. Golovanova, M.C. Spadaro, J. Arbiol, V. Golovanov, T.T. Rantala, T. Andreu, J. R. Morante, Effects of solar irradiation on thermally driven CO_2 methanation using Ni/CeO2–based catalyst, Appl. Catal. B 291 (2021) 120038, https://doi.org/10.1016/j.apcatb.2021.120038.

[17] S. Ullah, E.C. Lovell, T.H. Tan, B. Xie, P.V. Kumar, R. Amal, J. Scott, Photoenhanced CO_2 methanation over La2O3 promoted Co/TiO2 catalysts, Appl. Catal. B 294 (2021), 120248, https://doi.org/10.1016/j.apcatb.2021.120248.

[18] J. Ashok, M.L. Ang, S. Kawi, Enhanced activity of CO_2 methanation over Ni/CeO2-ZrO2 catalysts: influence of preparation methods, Catal. Today 281 (2017) 304–311, https://doi.org/10.1016/j.cattod.2016.07.020.

[19] M. Kumar, J.-H. Yun, V. Bhatt, B. Singh, J. Kim, J.-S. Kim, B.S. Kim, C.Y. Lee, Role of Ce3+ valence state and surface oxygen vacancies on enhanced electrochemical performance of single step solvothermally synthesized CeO2 nanoparticles, Electro Acta 284 (2018) 709–720, https://doi.org/10.1016/j.electacta.2018.07.184.

[20] C. Kim, S. Hyeon, J. Lee, W.D. Kim, D.C. Lee, J. Kim, H. Lee, Energy-efficient CO 2 hydrogenation with fast response using photoexcitation of CO 2 adsorbed on metal catalysts, Nat. Commun. 9 (2018) 1–8, https://doi.org/10.1038/s41467-018-05542-5.

[21] M. Xiao, X. Zhang, Y. Yang, X. Cui, T. Chen, Y. Wang, M (M= Mn, Co, Cu)-CeO2 catalysts to enhance their CO catalytic oxidation at low temperature: synergistic effects of the interaction between Ce3+-Mx+-Ce4+ and the oxygen vacancy defects, Fuel 323 (2022), 124379, https://doi.org/10.1016/j.fuel.2022.124379.

[22] L. Mädler, H.K. Kammler, R. Mueller, S.E. Pratsinis, Controlled synthesis of nanostructured particles by flame spray pyrolysis, J. Aerosol Sci. 33 (2002) 369–389, https://doi.org/10.1016/S0021-8502(01)00159-8.

[23] P.E. Blöchl, Projector augmented-wave method, Phys. Rev. B 50 (1994) 17953–17979, https://doi.org/10.1103/PhysRevB.50.17953.

[24] G. Kresse, D. Joubert, From ultrasoft pseudopotentials to the projector augmented-wave method, Phys. Rev. B 59 (1999) 1758–1775, https://doi.org/10.1103/PhysRevB.59.1758.

[25] G. Kresse, J. Furthmüller, Efficiency of ab-initio total energy calculations for metals and semiconductors using a plane-wave basis set, Comput. Mater. Sci. 6 (1996) 15–50, https://doi.org/10.1016/0927-0256(96)00008-0.

[26] G. Kresse, J. Furthmüller, Efficient iterative schemes for ab initio total-energy calculations using a plane-wave basis set, Phys. Rev. B 54 (1996) 11169–11186, https://doi.org/10.1103/PhysRevB.54.11169.

[27] J.P. Perdew, K. Burke, M. Ernzerhof, Generalized gradient approximation made simple, Phys. Rev. Lett. 77 (1996) 3865–3868, https://doi.org/10.1103/PhysRevLett.77.3865.

[28] S.L. Dudarev, G.A. Botton, S.Y. Savrasov, C.J. Humphreys, A.P. Sutton, Electron-energy-loss spectra and the structural stability of nickel oxide: an LSDA+U study, Phys. Rev. B 57 (1998) 1505–1509, https://doi.org/10.1103/PhysRevB.57.1505.

[29] R. Kydd, W.Y. Teoh, K. Wong, Y. Wang, J. Scott, Q. Zeng, A. Yu, J. Zou, R. Amal, Flame-synthesized ceria-supported copper dimers for preferential oxidation of CO, Adv. Funct. Mater. 19 (2009) 369–377, https://doi.org/10.1002/adfm.200801211.

[30] L. Mädler, W.J. Stark, S.E. Pratsinis, Flame-made ceria nanoparticles, J. Mater. Res. 17 (2002) 1356–1362, https://doi.org/10.1557/JMR.2002.0202.

[31] M. Thommes, K. Kaneko, A.V. Neimark, J.P. Olivier, F. Rodriguez-Reinoso, J. Rouquerol, K.S.W. Sing, Physisorption of gases, with special reference to the evaluation of surface area and pore size distribution (IUPAC Technical Report), Pure Appl. Chem. 87 (2015) 1051–1069, https://doi.org/10.1515/pac-2014-1117.

[32] E.C. Lovell, J. Horlyck, J. Scott, R. Amal, Flame spray pyrolysis-designed silica/ceria-zirconia supports for the carbon dioxide reforming of methane, Appl. Catal. A Gen. 546 (2017) 47–57, https://doi.org/10.1016/j.apcata.2017.08.002.

[33] W.Y. Teoh, F. Denny, R. Amal, D. Friedmann, L. Mädler, S.E. Pratsinis, Photocatalytic mineralisation of organic compounds: a comparison of flame-made TiO 2 catalysts, Top. Catal. 44 (2007) 489–497, https://doi.org/10.1007/s11244-006-0096-4.

[34] E. Clementi, D.L. Raimondi, W.P. Reinhardt, Atomic screening constants from SCF functions. II. Atoms with 37 to 86 electrons, J. Chem. Phys. 47 (1967) 1300–1307, https://doi.org/10.1063/1.1712084.

[35] H. Yu, R. Xin, X. Zhang, H. Liu, K. Zheng, J. Zhao, L. Zhan, C. Xu, W. Wan, Y. Zhu, J. Huo, Crystallization behavior, quantitation of Ce3+/Ce4+ and chemical stability analysis of multiple alkaline earths borosilicate glasses for immobilizing simulated tetravalent actinides, J. Non Cryst. Solids 558 (2021), 120642, https://doi.org/10.1016/j.jnoncrysol.2021.120642.

[36] S. Sharma, Z. Hu, P. Zhang, E.W. McFarland, H. Metiu, CO_2 methanation on Ru-doped ceria, J. Catal. 278 (2011) 297–309, https://doi.org/10.1016/j.jcat.2010.12.015.

[37] C. Suryanarayana, M.G. Norton, X-rays and Diffraction, in: X-Ray Diffraction, Springer, 1998, pp. 3–19.

[38] A. Cárdenas-Arenas, A. Quindimil, A. Davó-Quiñonero, E. Bailón-García, D. Lozano-Castello, U. De-La-Torre, B. Pereda-Ayo, J.A. González-Marcos, J. R. González-Velasco, A. Bueno-López, Isotopic and in situ DRIFTS study of the CO_2 methanation mechanism using Ni/CeO2 and Ni/Al2O3 catalysts, Appl. Catal. B 265 (2020), 118538, https://doi.org/10.1016/j.apcatb.2019.118538.

[39] A. Parastaev, V. Muravev, E. Huertas Osta, A.J.F. van Hoof, T.F. Kimpel, N. Kosinov, E.J.M. Hensen, Boosting CO_2 hydrogenation via size-dependent metal–support interactions in cobalt/ceria-based catalysts, Nat. Catal. 3 (2020) 526–533, https://doi.org/10.1038/s41929-020-0459-4.

[40] W. Karim, C. Spreafico, A. Kleibert, J. Gobrecht, J. VandeVondele, Y. Ekinci, J. A. van Bokhoven, Catalyst support effects on hydrogen spillover, Nature 541 (2017) 68–71, https://doi.org/10.1038/nature20782.

[41] Z. Liu, J. Li, M. Buettner, R.V. Ranganathan, M. Uddi, R. Wang, Metal–support interactions in CeO2- and SiO2-supported cobalt catalysts: effect of support morphology, reducibility, and interfacial configuration, ACS Appl. Mater. Interfaces 11 (2019) 17035–17049, https://doi.org/10.1021/acsami.9b02455.

[42] M. Li, H. Amari, A.C. van Veen, Metal-oxide interaction enhanced CO_2 activation in methanation over ceria supported nickel nanocrystallites, Appl. Catal. B 239 (2018) 27–35, https://doi.org/10.1016/j.apcatb.2018.07.074.

[43] A. Parastaev, V. Muravev, E.H. Osta, T.F. Kimpel, J.F.M. Simons, A.J.F. van Hoof, E. Uslamin, L. Zhang, J.J.C. Struijs, D.B. Burueva, E.V. Pokochueva, K.V. Kovtunov, I.V. Koptyug, I.J. Villar-Garcia, C. Escudero, T. Altantzis, P. Liu, A. Béché, S. Bals, N. Kosinov, E.J.M. Hensen, Breaking structure sensitivity in CO_2 hydrogenation by tuning metal–oxide interfaces in supported cobalt nanoparticles, Nat. Catal. 5 (2022) 1051–1060, https://doi.org/10.1038/s41929-022-00874-4.

[44] M. Minnermann, H.K. Grossmann, S. Pokhrel, K. Thiel, H. Hagelin-Weaver, M. Bäumer, L. Mädler, Double flame spray pyrolysis as a novel technique to synthesize alumina-supported cobalt Fischer–Tropsch catalysts, Catal. Today 214 (2013) 90–99, https://doi.org/10.1016/j.cattod.2013.04.001.

[45] E. Petryayeva, U.J. Krull, Localized surface plasmon resonance: nanostructures, bioassays and biosensing—A review, Anal. Chim. Acta 706 (2011) 8–24, https://doi.org/10.1016/j.aca.2011.08.020.

[46] N.A.M. Barakat, M.S. Khil, F.A. Sheikh, H.Y. Kim, Synthesis and optical properties of two cobalt oxides (CoO and Co3O4) nanofibers produced by electrospinning process, J. Phys. Chem. C. 112 (2008) 12225–12233, https://doi.org/10.1021/jp8027353.

[47] J. Shi, H. Li, A. Genest, W. Zhao, P. Qi, T. Wang, G. Rupprechter, High-performance water gas shift induced by asymmetric oxygen vacancies: gold clusters supported by ceria-praseodymia mixed oxides, Appl. Catal. B 301 (2022), 120789, https://doi.org/10.1016/j.apcatb.2021.120789.

[48] E. Bêche, P. Charvin, D. Perarnau, S. Abanades, G. Flamant, Ce 3d XPS investigation of cerium oxides and mixed cerium oxide (CexTiyOz), Surf. Interface Anal. 40 (2008) 264–267, https://doi.org/10.1002/sia.2686.

[49] Q. Yao, L. Zhang, D. Huang, Q. Ding, W. Feng, J. Zhang, Y. Ren, X. Chen, B. Yue, H. He, MAS NMR studies on the formation and structure of oxygen vacancy on the CeO2 {110} surface under a reducing atmosphere, J. Phys. Chem. C. (2023), https://doi.org/10.1021/acs.jpcc.3c02592.

[50] S.S.-Y. Lin, D.H. Kim, M.H. Engelhard, S.Y. Ha, Water-induced formation of cobalt oxides over supported cobalt/ceria–zirconia catalysts under ethanol-steam conditions, J. Catal. 273 (2010) 229–235, https://doi.org/10.1016/j.jcat.2010.05.016.

[51] A. Efremova, I. Szenti, J. Kiss, Á. Szamosvölgyi, A. Sápi, K. Baán, L. Olivi, G. Varga, Z. Fogarassy, B. Pécz, Á. Kukovecz, Z. Kónya, Nature of the Pt-Cobalt-Oxide surface interaction and its role in the CO_2 Methanation, Appl. Surf. Sci. 571 (2022), 151326, https://doi.org/10.1016/j.apsusc.2021.151326.

[52] G. Greczynski, L. Hultman, X-ray photoelectron spectroscopy: towards reliable binding energy referencing, Prog. Mater. Sci. 107 (2020) 100591, https://doi.org/10.1016/j.pmatsci.2019.100591.

[53] E. Villa-Aleman, A.L. Houk, D.D. Dick, S.E. Hunyadi Murph, Hyper-Raman spectroscopy of CeO2, J. Raman Spectrosc. 51 (2020) 1260–1263, https://doi.org/10.1002/jrs.5886.

[54] K.C. Remani, N.N. Binitha, Cobalt doped ceria catalysts for the oxidative abatement of gaseous pollutants and colorimetric detection of H2O2, Mater. Res. Bull. 139 (2021), 111253, https://doi.org/10.1016/j.materresbull.2021.111253.

[55] F. Morfin, T.-S. Nguyen, J.-L. Rousset, L. Piccolo, Synergy between hydrogen and ceria in Pt-catalyzed CO oxidation: an investigation on Pt–CeO2 catalysts synthesized by solution combustion, Appl. Catal. B 197 (2016) 2–13, https://doi.org/10.1016/j.apcatb.2016.01.056.

[56] X. Qin, M. Chen, X. Chen, J. Zhang, X. Wang, J. Fang, C. Zhang, Effects of the metal–support interaction in Ru/CeO2 nanostructures on active oxygen species for HCHO/CO oxidation, ACS Appl. Nano Mater. 5 (2022) 15574–15582, https://doi.org/10.1021/acsanm.2c03623.

[57] N. Wang, W. Qian, W. Chu, F. Wei, Crystal-plane effect of nanoscale CeO2 on the catalytic performance of Ni/CeO2 catalysts for methane dry reforming, Catal. Sci. Technol. 6 (2016) 3594–3605, https://doi.org/10.1039/C5CY01790D.

[58] S. Loridant, Raman spectroscopy as a powerful tool to characterize ceria-based catalysts, Catal. Today 373 (2021) 98–111, https://doi.org/10.1016/j.cattod.2020.03.044.

[59] G. Grzybek, P. Stelmachowski, S. Gudyka, P. Indyka, Z. Sojka, N. Guillén-Hurtado, V. Rico-Pérez, A. Bueno-López, A. Kotarba, Strong dispersion effect of cobalt spinel active phase spread over ceria for catalytic N2O decomposition: the role of the

interface periphery, Appl. Catal. B 180 (2016) 622–629, https://doi.org/10.1016/j.apcatb.2015.07.027.

[60] G. Varvoutis, M. Lykaki, S. Stefa, V. Binas, G.E. Marnellos, M. Konsolakis, Deciphering the role of Ni particle size and nickel-ceria interfacial perimeter in the low-temperature CO_2 methanation reaction over remarkably active Ni/CeO2 nanorods, Appl. Catal. B 297 (2021), 120401, https://doi.org/10.1016/j.apcatb.2021.120401.

[61] E.T. Kho, T.H. Tan, E. Lovell, R.J. Wong, J. Scott, R. Amal, A review on photo-thermal catalytic conversion of carbon dioxide, Green. Energy Environ. 2 (2017) 204–217, https://doi.org/10.1016/j.gee.2017.06.003.

[62] T. Schaaf, J. Grünig, M.R. Schuster, T. Rothenfluh, A. Orth, Methanation of CO 2-storage of renewable energy in a gas distribution system, Energy Sustain Soc. 4 (2014) 1–14, https://doi.org/10.1186/s13705-014-0029-1.

[63] M. González-Castaño, B. Dorneanu, H. Arellano-García, The reverse water gas shift reaction: a process systems engineering perspective, React. Chem. Eng. 6 (2021) 954–976, https://doi.org/10.1039/D0RE00478B.

[64] M.A.A. Aziz, A.A. Jalil, S. Triwahyono, A. Ahmad, CO_2 methanation over heterogeneous catalysts: recent progress and future prospects, Green. Chem. 17 (2015) 2647–2663, https://doi.org/10.1039/C5GC00119F.

[65] H. Robatjazi, J.L. Bao, M. Zhang, L. Zhou, P. Christopher, E.A. Carter, P. Nordlander, N.J. Halas, Plasmon-driven carbon–fluorine (C(sp3)–F) bond activation with mechanistic insights into hot-carrier-mediated pathways, Nat. Catal. 3 (2020) 564–573, https://doi.org/10.1038/s41929-020-0466-5.

[66] O. Pozdnyakova, D. Teschner, A. Wootsch, J. Kröhnert, B. Steinhauer, H. Sauer, L. Toth, F.C. Jentoft, A. Knop-Gericke, Z. Paál, Preferential CO oxidation in hydrogen (PROX) on ceria-supported catalysts, part II: oxidation states and surface species on Pd/CeO2 under reaction conditions, suggested reaction mechanism, J. Catal. 237 (2006) 17–28, https://doi.org/10.1016/j.jcat.2005.10.015.

[67] C. Binet, A. Badri, M. Boutonnet-Kizling, J.-C. Lavalley, FTIR study of carbon monoxide adsorption on ceria: CO 2–2 carbonite dianion adsorbed species, J. Chem. Soc. Faraday Trans. 90 (1994) 1023–1028, https://doi.org/10.1039/FT9949001023.

[68] T.H. Nguyen, H.B. Kim, E.D. Park, CO and CO_2 methanation over CeO2-supported cobalt catalysts, Catalysts 12 (2022) 212, https://doi.org/10.3390/catal12020212.

[69] K. Deng, L. Lin, N. Rui, D. Vovchok, F. Zhang, S. Zhang, S.D. Senanayake, T. Kim, J. A. Rodriguez, Studies of CO 2 hydrogenation over cobalt/ceria catalysts with in situ characterization: the effect of cobalt loading and metal–support interactions on the catalytic activity, Catal. Sci. Technol. 10 (2020) 6468–6482, https://doi.org/10.1039/D0CY00962H.

[70] C. Binet, M. Daturi, J.-C. Lavalley, IR study of polycrystalline ceria properties in oxidised and reduced states, Catal. Today 50 (1999) 207–225, https://doi.org/10.1016/S0920-5861(98)00504-5.

[71] J. Li, Y. Lin, X. Pan, D. Miao, D. Ding, Y. Cui, J. Dong, X. Bao, Enhanced CO_2 methanation activity of Ni/anatase catalyst by tuning strong metal–support interactions, ACS Catal. 9 (2019) 6342–6348, https://doi.org/10.1021/acscatal.9b00401.

[72] G.N. Vayssilov, M. Mihaylov, P.S. Petkov, K.I. Hadjiivanov, K.M. Neyman, Reassignment of the vibrational spectra of carbonates, formates, and related surface species on ceria: a combined density functional and infrared spectroscopy investigation, J. Phys. Chem. C. 115 (2011) 23435–23454, https://doi.org/10.1021/jp208050a.

[73] P.G. Lustemberg, M.V. Bosco, A. Bonivardi, H.F. Busnengo, M.V. Ganduglia-Pirovano, Insights into the nature of formate species in the decomposition and reaction of methanol over cerium oxide surfaces: a combined infrared spectroscopy and density functional theory study, J. Phys. Chem. C. 119 (2015) 21452–21464, https://doi.org/10.1021/acs.jpcc.5b05070.

[74] S. Kattel, B. Yan, Y. Yang, J.G. Chen, P. Liu, Optimizing binding energies of key intermediates for CO_2 hydrogenation to methanol over oxide-supported copper, J. Am. Chem. Soc. 138 (2016) 12440–12450, https://doi.org/10.1021/jacs.6b05791.

[75] C. Wu, L. Lin, J. Liu, J. Zhang, F. Zhang, T. Zhou, N. Rui, S. Yao, Y. Deng, F. Yang, Inverse ZrO2/Cu as a highly efficient methanol synthesis catalyst from CO_2 hydrogenation, Nat. Commun. 11 (2020) 1–10, https://doi.org/10.1038/s41467-020-19634-8.

[76] J. Wang, G. Li, Z. Li, C. Tang, Z. Feng, H. An, H. Liu, T. Liu, C. Li, A highly selective and stable ZnO-ZrO2 solid solution catalyst for CO_2 hydrogenation to methanol, Sci. Adv. 3 (2017), e1701290, https://doi.org/10.1126/sciadv.1701290.

[77] I.C. ten Have, J.J.G. Kromwijk, M. Monai, D. Ferri, E.B. Sterk, F. Meirer, B. M. Weckhuysen, Uncovering the reaction mechanism behind CoO as active phase for CO_2 hydrogenation, Nat. Commun. 13 (2022) 324, https://doi.org/10.1038/s41467-022-27981-x.

[78] C. Liang, H. Tian, G. Gao, S. Zhang, Q. Liu, D. Dong, X. Hu, Methanation of CO_2 over alumina supported nickel or cobalt catalysts: effects of the coordination between metal and support on formation of the reaction intermediates, Int J. Hydrog. Energy 45 (2020) 531–543, https://doi.org/10.1016/j.ijhydene.2019.10.195.

[79] P.A.U. Aldana, F. Ocampo, K. Kobl, B. Louis, F. Thibault-Starzyk, M. Daturi, P. Bazin, S. Thomas, A.C. Roger, Catalytic CO_2 valorization into CH4 on Ni-based ceria-zirconia. Reaction mechanism by operando IR spectroscopy, Catal. Today 215 (2013) 201–207, https://doi.org/10.1016/j.cattod.2013.02.019.

[80] L.M.N.C. Alves, M.P. Almeida, M. Ayala, C.D. Watson, G. Jacobs, R.C. Rabelo-Neto, F.B. Noronha, L.V. Mattos, CO_2 methanation over metal catalysts supported on ZrO2: effect of the nature of the metallic phase on catalytic performance, Chem. Eng. Sci. 239 (2021), 116604, https://doi.org/10.1016/j.ces.2021.116604.